RSC Advances

PAPER

View Article Online
View Journal | View Issue

Cite this: *RSC Adv.*, 2026, **16**, 13083

Bridging first-principles calculations and device simulations of A_3GaI_6 (A = K, Rb, Cs) double perovskites for next-generation solar cells: DFT, AIMD, and SCAPS-1D

Muhammad Awais Jehangir,[a] Selma Rabhi, *[b] Rachid Makhloufi,[c] Asadul Islam Shimul, *[d] Asif Nawaz Khan,[e] Yaacoub Ibrahim Bouderbala,[f] Omar H. Alsalmi,[g] Shima Sadaf[h] and Mir Waqas Alam *[i]

Halide perovskites have garnered significant interest as advanced materials for optoelectronic applications and energy harvesting devices, owing to their adjustable bandgaps, elevated absorption coefficients, and exceptional charge transport characteristics. Among them, double perovskites of the less explored formula, specifically A_3BX_6-type halide double perovskites, remain relatively underrepresented in the literature. In this work, the structural, mechanical, thermodynamic, electronic, optical, and thermoelectrical properties of the lead-free halide perovskites A_3GaI_6 (A = Cs, K, Rb) were systematically investigated using first-principles calculations within the WIEN2k framework employing GGA-PBE, TB-mBJ, and TB-mBJ+SOC functionals. Structural stability was confirmed through Goldschmidt tolerance factors, negative formation energies, convex-hull analysis, and elastic constants. The calculated direct band gaps based on both functionals (TB-mBJ/TB-mBJ+SOC) of 2.06/1.88 eV (Cs_3GaI_6), 1.83/1.65 eV (K_3GaI_6), and 1.94/1.76 eV (Rb_3GaI_6) indicate strong optical absorption in the visible to near-infrared region. Carrier-density and Bader-charge analyses reveal that the Ga–I framework governs electronic transport, while the A-site cations tune the charge distribution, with K_3GaI_6 and Rb_3GaI_6 exhibiting higher carrier densities and stronger charge transfer than Cs_3GaI_6. Among the studied compounds, K_3GaI_6 possesses the most suitable band gap (~1.65 eV), lower carrier effective masses, higher carrier mobilities, and a larger static dielectric constant, indicating efficient charge separation and transport, and thus superior photovoltaic potential. Based on DFT-derived parameters, SCAPS-1D simulations of sixteen n-i-p device architectures based on K_3GaI_6 yield power conversion efficiencies ranging from 19.48% to 22.48%, with the AZO/STO/K_3GaI_6/Zn_2P_2 configuration showing the best performance due to favorable band alignment and transport-layer properties. After optimization, the efficiency reaches 27.19%, highlighting K_3GaI_6 as a highly promising lead-free absorber for high-performance perovskite solar cells. This work establishes a direct link between material properties and device performance and provides a solid theoretical foundation for the experimental realization of A_3GaI_6-based optoelectronic and energy-harvesting applications.

Received 9th December 2025
Accepted 4th March 2026

DOI: 10.1039/d5ra09544a

rsc.li/rsc-advances

1. Introduction

Finding sustainable and renewable energy sources has become more important due to the world's rapidly increasing energy consumption and the pressing need to slow down climate change.[1] Since solar energy is abundant and environmentally friendly, it is regarded as one of the most promising options among them. In recent years, metal halide perovskites have

[a]*Institute of Fundamental and Frontier Sciences, University of Electronic Science and Technology of China, Chengdu, Sichuan 611731, China*

[b]*Laboratory of Innovative Environmental Preservation Techniques, Department of Chemistry, Constantine 1 University, 25000 Constantine, Algeria. E-mail: selma.rabhi@umc.edu.dz*

[c]*Laboratory of Applied Chemistry (LCA), University of Biskra, P.O. Box 145, 07000 Biskra, Algeria*

[d]*Department of Electrical and Electronic Engineering, Gopalganj Science and Technology University, Gopalganj-8100, Bangladesh. E-mail: shimul.18eee009@gstu.edu.bd*

[e]*Department of Physics, University of Science & Technology Bannu, 28100 Khyber Pakhtunkhwa, Pakistan*

[f]*Applied Optics Laboratory, Institute of Optics and Precision Mechanics, University of Ferhat Abbas, 19000 Setif, Algeria*

[g]*Department of Physics, College of Science, Umm Al-Qura University, Makkah 21955, Saudi Arabia*

[h]*Department of Electrical Engineering, College of Engineering King Faisal University, Al-Ahsa 31982, Saudi Arabia*

[i]*Department of Physics, College of Science, King Faisal University, Al-Ahsa 31982, Saudi Arabia. E-mail: wmir@kfu.edu.sa*

attracted significant attention in photovoltaic research owing to their exceptional optoelectronic properties, such as tunable band gaps, high absorption coefficients, long carrier diffusion lengths, and solution-processable fabrication routes.[2–4] These features have enabled perovskite solar cells (PSCs) to achieve remarkable power conversion efficiencies (PCEs) exceeding 26.95%,[5] rivaling or surpassing those of established technologies such as silicon-based photovoltaics. Unfortunately, the inherent problems with typical lead halide perovskites, such as their toxicity to the environment and long-term stability problems, prevent them from being widely commercialized.[6–9] To address these challenges, considerable research efforts have focused on lead-free halide perovskites and double perovskite derivatives, offering improved chemical stability and reduced toxicity while maintaining desirable optoelectronic characteristics. In this context, double perovskites have recently emerged as potential alternatives, where DFT calculations suggest that these compounds exhibit direct band gaps in the range of 1.6–2.1 eV, making them well-suited for visible-light absorption.[10–12] Their favorable dielectric responses, refractive indices, and absorption coefficients further highlight their potential for optoelectronic applications, particularly in solar energy harvesting. Recent research has shown that $Cs_2AgBiBr_6$ is a promising substitute for the new lead-based perovskites in solar cell applications,[13,14] these substances show excellent photovoltaic performance and are investigated further in experiments. Cesium-based compounds including $Cs_2NaBiBr_6$, $Cs_2InBiBr_6$, $Cs_2AgBiBr_6$, $KBaTeBiO_6$, and $Cs_2CuBiBr_6$ have shown potential efficiencies for solar energy conversion, however there are still few experimental studies of halide double perovskites (HDPs).[15,16] Compared to the well-explored $A_2BB'X_6$ double halide perovskites, where A is a monovalent cation, B and B′ are metal cations, and X is a halide or halogen element, the A_3BX_6 structure remains relatively less studied. Early work by Rakhmatullin *et al.*[17] reported the synthesis and characterization of Rb_3ScF_6 for the first time, followed by Morrison *et al.*, who successfully grew single crystals of A_3MF_6 (A = Rb, Cs; M = Al, Ga) using mixed alkali chloride/fluoride fluxes in sealed silver tubes.[18] On the theoretical side, the structure of Cs_3GaF_6 (Material Project ID: mp-1113508) has been investigated, providing initial insights into this family. Recent progress in lead-free photovoltaic absorbers has been strongly supported by both experimental based on first-principles investigations. For instance, Crovetto *et al.*[19] systematically grew and characterized Cu_3BiI_6 solar cells using a unified synthesis and analysis protocol, enabling a direct comparison of their individual strengths, limitations, and shared challenges in device integration. Similarly, Baranwal *et al.*[20] fabricated a series of lead-free absorber layers, including Ag_3BiI_6, and evaluated their photovoltaic performance in both conventional (n-i-p) and inverted (p-i-n) architectures. Their results showed that although the n-i-p configuration generally yields higher efficiencies, the device performance is strongly affected by surface morphology and interface quality, which depend on the underlying transport layer. These studies highlight that, beyond suitable band gaps, the optimization of transport properties, interface alignment, and defect control is essential for achieving high-efficiency and environmentally friendly solar cells. Despite the rapid progress in lead-free halide perovskites, the A_3BX_6-type iodide compounds remain largely unexplored, and no comprehensive study has yet connected their fundamental properties with device-level photovoltaic performance. In particular, A_3GaI_6 (A = K, Rb, Cs) has not previously been investigated for solar-cell applications, and the lack of experimental and theoretical data on their optoelectronic and transport properties represents a clear research gap. In this work, a systematic and integrated approach is employed in which first-principles calculations are used to evaluate the structural, mechanical, thermodynamic, electronic, and optical properties, followed by SCAPS-1D device simulations based on the DFT-derived parameters. This multiscale strategy enables, for the first time, a direct link between material-level characteristics and photovoltaic performance for this family of compounds. The novelty of the present study lies in (i) the first detailed investigation of iodide A_3GaI_6 (A = K, Rb, Cs) perovskites using the TB-mBJ+SOC approach, (ii) the identification of K_3GaI_6 as the most suitable absorber based on a comprehensive analysis of band gap, carrier transport, dielectric response, and device compatibility, and (iii) the design of sixteen K_3GaI_6-based devices and the optimization of a high-efficiency n-i-p solar-cell architecture achieving a PCE of 27.19%. These results provide a new pathway for the development of environmentally friendly perovskite absorbers and establish a theoretical foundation for their future experimental realization and integration into next-generation optoelectronic devices.

2. Calculation methodology and settings

The structural stability and energy-volume behavior of the studied compounds were analyzed by fitting total energy *versus* volume data using the Birch–Murnaghan equation of state (EOS),[21] which is widely recognized for its accuracy and applicability across a range of materials. Key characteristics such as equilibrium volume, minimum energy, bulk modulus, and its pressure derivative might be determined using this method. DFT was used for first-principles calculations in the full-potential linearized augmented plane wave (FP-LAPW) framework, which is implemented in the WIEN2k software package.[22] The exchange-correlation energy was initially treated using the Perdew–Burke–Ernzerhof (PBE) form of the generalized gradient approximation (GGA). However, since conventional GGA functionals are known to systematically underestimate the band gap, the Tran–Blaha modified Becke–Johnson (TB-mBJ) potential was adopted to achieve more accurate predictions. Furthermore, the inclusion of spin–orbit coupling (SOC) in the TB-mBJ+SOC approach is particularly important for halide perovskites such as A_3GaI_6 (A = Cs, K, and Rb). SOC arises from the interaction between the electron's spin and its orbital motion in the electrostatic field of the nucleus and constitutes a key relativistic effect in materials containing heavy elements. In such systems, SOC significantly modifies the band dispersion, shifts the positions of the valence- and conduction-band

edges, and consequently affects the band-gap magnitude as well as the carrier effective masses. Therefore, incorporating SOC is essential for obtaining an accurate description of the electronic structure and optical response and for providing a more realistic prediction of the optoelectronic properties of these compounds. Several previous studies have also demonstrated the importance of SOC in halide double perovskites; for instance, Elfatouaki *et al.*[23] employed SOC in their investigation of the electronic properties of Cs_2AgBiI_6, while Khan *et al.*[24] applied the same approach to X_2ScInI_6 (X = K, Rb. The GGA functional controls the exchange-correlation energy in this hybrid technique (PBE-GGA+Tb-mBJ), and the TB-mBJ+SOC potential corrects the understated band gap, which is very useful for evaluating electrical and optical properties. Prior to the structural optimization and electronic-structure calculations, careful convergence tests were performed to ensure the accuracy of the computational parameters. The total energy was converged to 0.0001 Ry and the forces to 1 mRy/a.u. with respect to the basis-set size and *k*-point sampling. Different Monkhorst–Pack *k*-meshes were examined, and a 10 × 10 × 10 grid was found to provide well-converged total energies, with further increases in *k*-point density producing negligible changes. In addition, the plane-wave cut–off parameter (RMT × K_{max} = 8) and G_{max} = 12 were optimized, and higher values did not significantly affect the calculated total energy. These parameters were therefore adopted for all subsequent calculations as an optimal compromise between computational efficiency and numerical accuracy. The elastic constants were obtained using the IRelast package.[25] Additionally, *ab initio* molecular dynamics (AIMD) simulations were conducted using the Quantum ESPRESSO software to assess the thermal stability of the compounds, employing the Verlet integration algorithm to model ion dynamics.

Based on the DFT-derived parameters of A_3GaI_6 (A = K, Rb, Cs), we modeled and simulated A_3GaI_6-based perovskite solar cells to evaluate their photovoltaic performance. The simulation phase, carried out using SCAPS-1D, plays a crucial role in saving both time and resources prior to the experimental fabrication of these materials into solar cell devices.[26] SCAPS-1D operates by solving three fundamental partial differential equations that are central to semiconductor physics-namely, Poisson's equation, the continuity equation for electrons, and the continuity equation for holes (eqn (1)–(3)). These equations collectively describe the distribution and transport of charge carriers within the device, thereby enabling accurate prediction of its electrical behavior and efficiency.

$$\frac{\partial}{\partial x}\left(-\varepsilon(x)\frac{\partial V}{\partial x}\right) = q[p(x) - n(x) + N_D{}^{+}(x) - N_A{}^{-}(x) + p_t(x) - n_t(x)] \quad (1)$$

$$\frac{\partial n}{\partial t} = \frac{1}{q}\frac{\partial J_n}{\partial x} + G_n - R_n \quad (2)$$

$$\frac{\partial p}{\partial t} = \frac{1}{q}\frac{\partial J_p}{\partial x} + G_p - R_p \quad (3)$$

where: ε, V, q, $p(x)$, $n(x)$, $N_D{}^{+}(x)$, $N_A{}^{-}(x)$, $p_t(x)$, and $n_t(x)$ are dielectric permittivity, electric potential, electronic charge, free hole density, free electron density, donor density, acceptor density, trap density of holes, and trap density of electrons, respectively. These equations are solved by the program to analyze basic properties. Standard solar cell testing parameters, including a temperature of 300 K, one sun's radiation, and an integrated power density of 1000 W m^{-2} (AM1.5 G), were used for the simulations.[27]

3. Results and discussion

3.1 Evaluation of the stability of A_3GaI_6 (A = K, Rb, Cs) halide perovskites

The stability of materials like A_3GaI_6 (A = K, Rb, Cs) requires a detailed analysis of their mechanical, thermodynamic, and structural characteristics. The structural analysis shows that the lattice constants of the compounds under investigation and the size of their ionic radii are directly related. Using optimized lattice constants, the crystal structures of A_3GaI_6 (A = Cs, K, and Rb) compounds were produced. They were discovered to be stable in cubic phases with space group $Fm\bar{3}m$ (#225), Fig. 1 shows the generated crystal structures. The Wyckoff coordinates of Ga are (0, 0, 0), and A (A = K, Rb, Cs) are located at (0.25, 0.25, 0.25) in the unit cell structures of the materials provided; otherwise, (0, 0, 0.23) for I.

The optimal lattice parameters calculated by PBE-SOL-GGA are extracted using the Murnaghan equation of states, which documents the maximum energy release at the point of minimal volume. For the three compounds, Cs_3GaI_6, K_3GaI_6, and Rb_3GaI_6, the optimized crystalline energy *vs.* volume graphs are displayed in Fig. 2(a)–(c), while the corresponding polyhedral structures are shown on the right. The equilibrium unit cell volume (V), lattice parameter (a), bulk modulus (B), its pressure derivative (B'), and ground state energy (E_0) are some of the important structural characteristics that we were able to determine through this fitting process.

The lattice parameters of the double perovskites A_3GaI_6 (A = Cs, K, and Rb) are consistent with values found in the literature

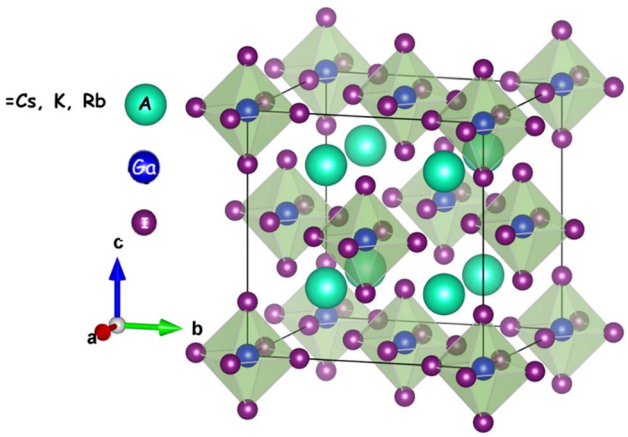

Fig. 1 Unit cell crystal structure of A_3GaI_6 (A = Cs, Rb and K).

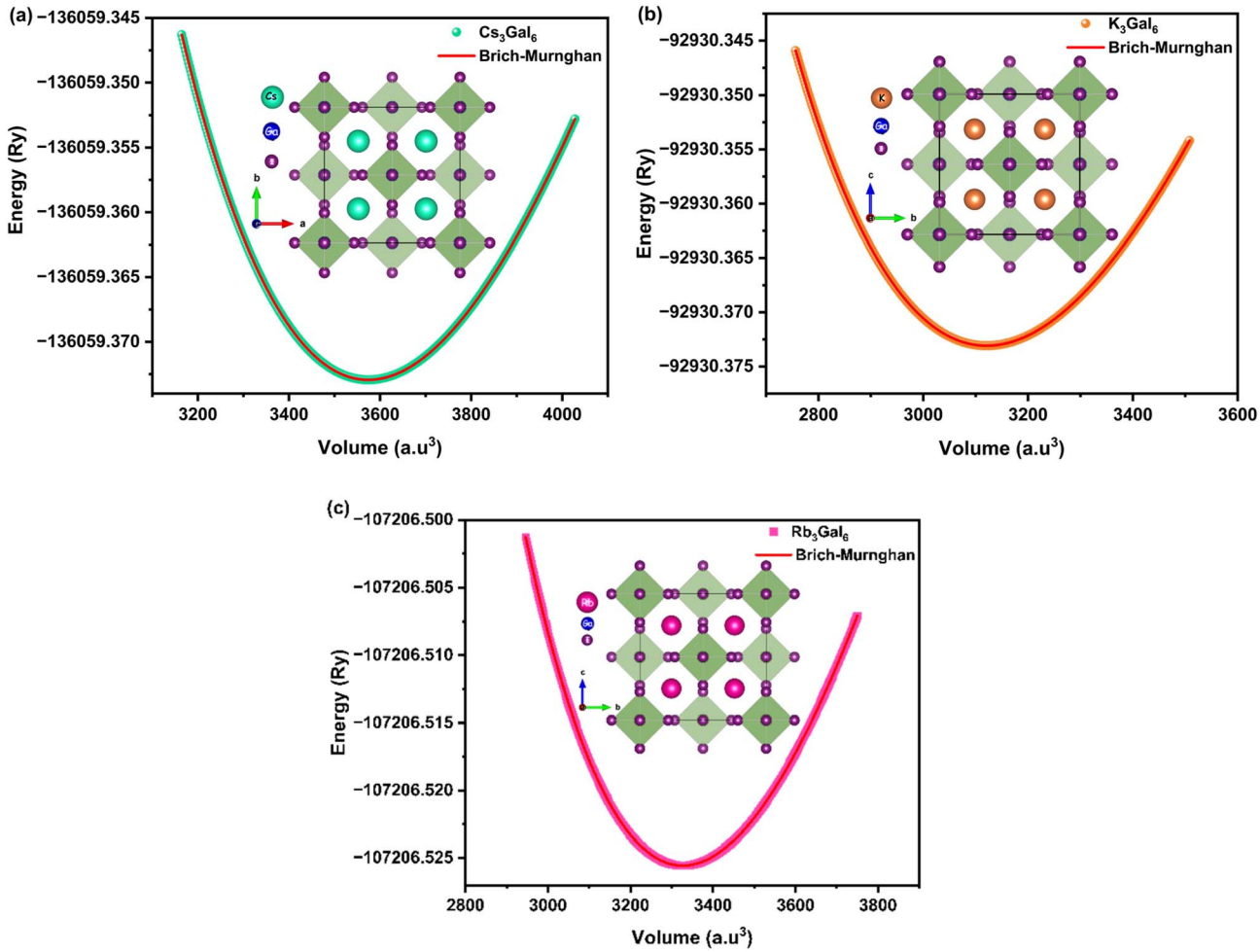

Fig. 2 Relationships between energy and volume for (a) Cs_3GaI_6, (b) K_3GaI_6, and (c) Rb_3GaI_6. The insets displayed the projection of the A_3GaI_6 (A = Cs, K, and Rb) structure on plan (100).

for comparable double perovskites,[25,26] where Table 1 included other A_3BI_6 for comparisons, which motivates further investigation into their properties due to the closer values between our compounds and that reported in literature. The lattice constants and cell volumes follow the expected trend based on the ionic radii of the A-site cations ($Cs^+ > Rb^+ > K^+$), with Cs_3GaI_6 exhibiting the largest lattice parameter (12.84 Å) and volume (3574.34 Å^3), and the highest density (3.86 g cm^{-3}). The calculated bulk modulus (B) values indicate moderate mechanical stability, with K_3GaI_6 showing the highest B (14.61 GPa), suggesting stronger resistance to compression compared to Cs_3GaI_6 (13.07 GPa) and Rb_3GaI_6 (12.84 GPa). On the other hand, the tolerance factor (τ) and octahedral factor (μ) were also evaluated using eqn (4) to assess structural stability, where all compounds show τ values between 0.93 and 0.97 and μ values between 0.41 and 0.57, indicating favorable geometries for forming a stable perovskite framework.[28,29]

$$\tau = \frac{\sqrt{2(r_A + r_I)}}{2r_{GA} + 2r_I} \text{ and } \mu = \frac{r_{GA}}{r_I} \quad (4)$$

where: r_A is Shannon ionic radii of Cs, K, and Rb extract it from VESTA.[30] Notably, the Goldschmidt tolerance factor (τ), which

Table 1 A_3GaI_6's computed structural, and energies parameters (A = Cs, K, and Rb)

	a_0 (Å)	V (Å^3)	ρ (g cm^{-3})	B (GPa)	B'	E_0 (R_y)	τ	μ	ΔH_f	E_{hull} (eV per at)
Cs_3GaI_6	12.84	3574.34	3.86	13.07	5.00	−136059.37	0.97	0.57	−1.22	0.117
K_3GaI_6	12.27	3121.10	3.41	14.61	5.00	−92930.37	0.93	0.56	−1.34	0.173
Rb_3GaI_6	12.54	3326.99	3.66	12.84	5.00	−107206.52	0.96	0.41	−1.31	0.090
Cs_3GaI_6 (ref. 33)	12.5627	1982.663	—	—	—	—	—	—	—	—
Cs_3SbCl_6 (ref. 2)	11.890	2836.302	2.896	18.611	5.00	−65248.106	1.0	—	−1.995	—

ideally ranges between 0.9 and 1.0 for cubic perovskite structures, suggests that these compounds are structurally compatible with a nearly ideal perovskite lattice.[28] All three compounds exhibit negative formation enthalpies, confirming their thermodynamic stability,[28,29] with K_3GaI_6 (−1.34 eV) being slightly more stable than Cs_3GaI_6 (−1.22 eV) and Rb_3GaI_6 (−1.31 eV). The ΔH_f was calculating using eqn (5).[31,32]

$$\Delta H_f = E_{tot}^{A_3GaI_6} - (3E_A^{Bulk} + E_{Ga}^{Bulk} + 6E_I^{Bulk}) \quad (5)$$

Compared A_3GaI_6 (A = Cs, K, and Rb) to others compounds such as Cs_3SbCl_6 which demonstrates superior mechanical (B = 18.61 GPa) and thermodynamic ($\Delta H_f = -1.995$ eV) stability (see Table 1), the Ga-based iodide perovskites present competitive properties, making them promising candidates for optoelectronic applications, particularly where heavier A-site cations contribute to improved structural robustness.

The A_3GaI_6 compounds (A = K, Rb, Cs) were further investigated for thermodynamic stability using the energy above the convex hull (E_{hull}) following the discussion of formation energies (E_f). This criterion is more stringent than the previous one, as it accounts for decomposition into all competing phases within the A-Ga-I chemical space. The hull energy of A_3GaI_6 is defined as.[34]

$$E_{hull}(A_3GaI_6) = E_{tot}(A_3GaI_6) - E_{hull}^{A\text{-}Ga\text{-}I}(3A + Ga + 6I) \quad (6)$$

where $E_{tot}(A_3GaI_6)$ denotes the total DFT energy of the optimized structure, and $E_{hull}^{A\text{-}Ga\text{-}I}$ corresponds to the minimum energy of the convex hull constructed from all relevant competing phases at the same overall composition. A value of $E_{hull} = 0$ indicates thermodynamic stability, while positive values signify metastability. The calculated hull energies show that K_3GaI_6 lies 0.173 eV per atom above the convex hull, indicating moderate metastability. In contrast, Cs_3GaI_6 exhibits lower hull energies of 0.117 eV per atom and 0.090 eV per atom for the two considered structural configurations, reflecting enhanced thermodynamic stability relative to Rb_3GaI_6. These values fall within the range commonly associated with experimentally accessible metastable halide compounds, suggesting that A_3GaI_6, particularly the Cs-based phases, may be realizable

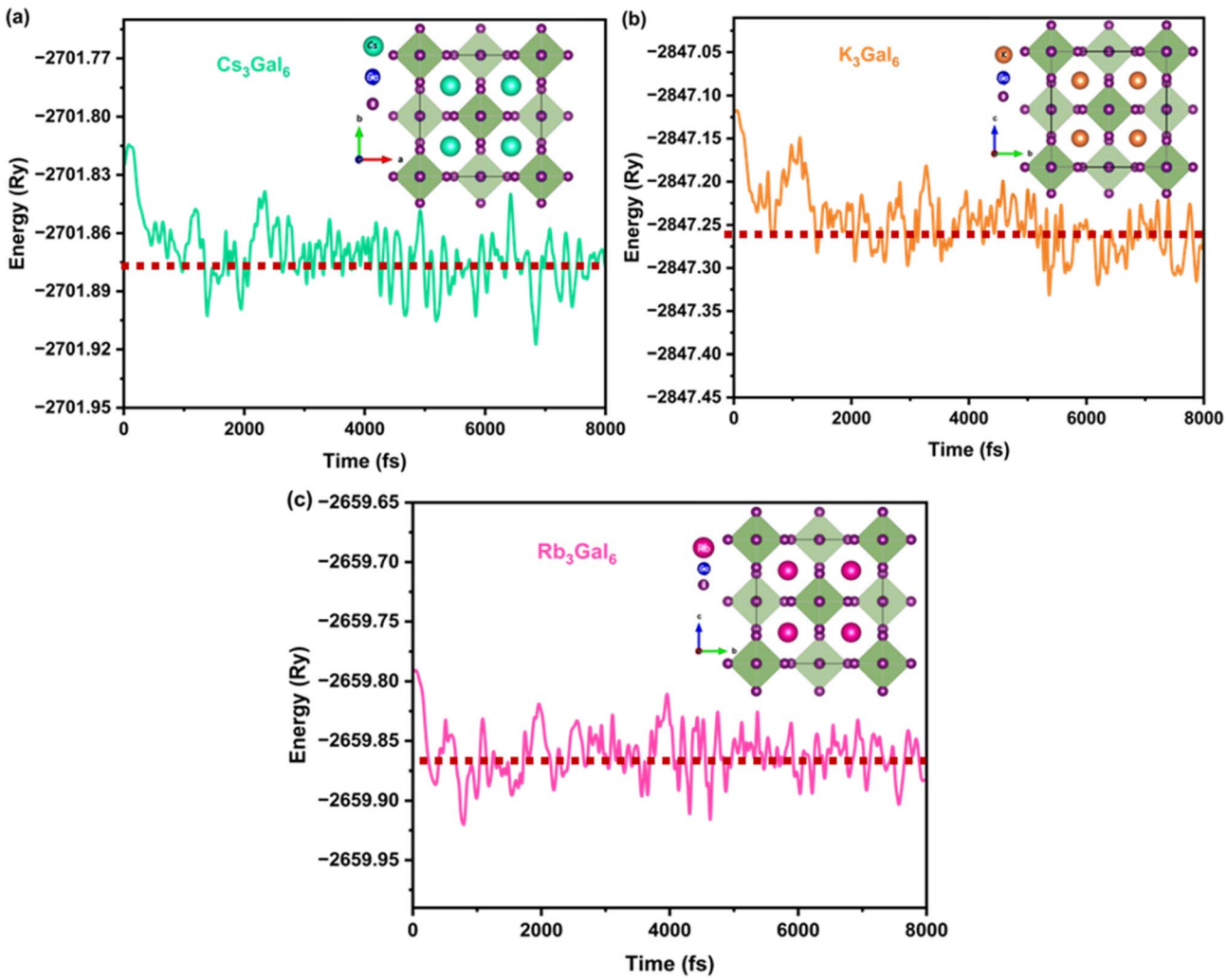

Fig. 3 Potential energy assessment during the *ab initio* molecular dynamic simulation (AIMD) period for (a) Cs_3GaI_6, (b) K_3GaI_6, and (c) Rb_3GaI_6.

under suitable synthesis conditions. Indeed, several perovskite-type compounds, such as the chalcogenide $SrZrS_3$, have been synthesized experimentally despite positive hull energies, illustrating that moderate thermodynamic metastability can be compatible with experimental realization.[34]

The thermodynamic stability of A_3GaI_6 (A = Cs, K, and Rb) was first evaluated from the negative formation energies. To further verify their thermal robustness, *ab initio* molecular dynamics (AIMD) simulations were performed at 300 K (Fig. 3). Initially, the potential energy exhibits significant fluctuations as a result of the thermalization process. After approximately 8000 fs, the energy fluctuations become confined within a narrow range around a constant average value, indicating that the systems have reached a dynamic equilibrium state. A horizontal line representing the mean potential energy has been added to the plots to clearly illustrate this equilibrium region. The absence of any systematic energy drift or structural degradation throughout the simulation confirms the thermal stability of all three compounds under ambient conditions, highlighting their suitability for practical device applications.[35]

The mechanical and thermomechanical properties of the halide double perovskites A_3GaI_6 (A = Cs, K, and Rb) were analyzed through their elastic constants and derived moduli to assess their stability, ductility, stiffness, and potential performance in devices. As listed in Table 2, the longitudinal constant C_{11} shows the trend K_3GaI_6 (15.35 GPa) ≈ Cs_3GaI_6 (14.95 GPa) > Rb_3GaI_6 (11.03 GPa), revealing that K_3GaI_6 and Cs_3GaI_6 possess stronger resistance to axial deformation, whereas Rb_3GaI_6 is significantly more compliant. A similar behavior is observed for the shear component C_{44}, where the markedly lower value for Rb_3GaI_6 (3.87 GPa) indicates weak resistance to shear strain and hence a softer mechanical response (see Table 2). The mechanical stability of A_2GaI_6 (A = K, Rb, Cs) was assessed using the Born stability criteria for cubic systems. The calculated elastic constants satisfy the required conditions $(C_{11} - C_{12}) > 0$, $C_{44} > 0$, $(C_{11} + 2C_{12}) > 0$, and $(C_{11} + 2C_{12}) > 0$, demonstrating that all compounds are mechanically stable as listed in Table 2. This confirms that the crystal structures are intrinsically stable against small elastic deformations. The bulk modulus and other derived moduli are therefore discussed only in terms of mechanical rigidity and resistance to compression.[36] The bulk modulus (B_H), shear modulus (G_H), and Young's modulus (Y_H) follow a decreasing trend from K → Cs → Rb, with K_3GaI_6 showing the highest values (B_H = 7.91 GPa, G_H = 6.13 GPa, Y_H = 14.62 GPa), indicating that it is the stiffest and most incompressible of the three, while Rb_3GaI_6 is the softest. To gain a better understanding, a number of polycrystalline elastic moduli, such as bulk modulus (B_H) and shear modulus (G_H), are calculated using the Hill approximation, which produces an average between the Voigt and Reuss bounds.[37,38] The bulk module (B_H) for cubic crystals is equal in the Voigt and Reuss approximations, and it can be written as follows using the Hill approximation:

$$B_H = B_V = B_V = (C_{11} + 2C_{12})/3 \quad (7)$$

The polycrystalline aggregates' shear modulus G_H, according to Hill, is

$$G = G_H = (G_V + G_R)/2 \quad (8)$$

where G_V is the shear modulus can be approximated according to Voigt and Reuss:

$$G_V = (C_{11} - C_{12} + 3C_{44})/5 \text{ and } G_R = \frac{5C_{44}(C_{11} - C_{12})}{4C_{44} + 3(C_{11} - C_{12})} \quad (9)$$

Furthermore, Poisson's ratio (ν_H) is lowest for Cs_3GaI_6 (0.18) and K_3GaI_6 (0.19), suggesting higher covalent bonding character, and a brittle character, whereas Rb_3GaI_6 shows a higher ν_H (0.26), indicating a more ionic bonding nature associated with ductile behavior.[39] Furthermore, this is further supported by the Cauchy pressure ($C_{12} - C_{44}$), which is slightly positive for Rb_3GaI_6, suggesting increased ionic character with ductile behavior according to Poisson's ratio, and negative for K_3GaI_6 and Cs_3GaI_6, indicating directional covalent bonding with brittle character according to results found from Poisso's ratio.[40] In other hand, the same behavior as Poisson ratio and Cauchy pressure, Pugh's ratio (B_H/G_H), often used to estimate ductility, suggests that all three compounds are brittle since $B_H/G_H < 1.75$ for K_3GaI_6 (1.29) and Cs_3GaI_6 (1.24), while Rb_3GaI_6 is

Table 2 For A_3GaI_6 (A = K, Rb, Cs), the calculated stiffness constants (C_{ij}, GPa) and the mechanical properties with the extreme values of elastic moduli, Poisson's ratio, and linear compressibility were obtained

Compounds		Cs_3GaI_6	K_3GaI_6	Rb_3GaI_6
C_{11}		14.95	15.35	11.03
C_{12}		3.61	4.19	4.39
C_{44}		6.11	6.53	3.87
Born criteria	$(C_{11} - C_{12}) > 0$	11.34	11.16	6.64
	$C_{44} > 0$	6.11 > 0	6.53 > 0	3.87 > 0
	$(C_{11} + 2C_{12}) > 0$	22.17	23.73	19.81
Bulk modulus B_H [GPa]		7.39	7.91	6.60
Shear modulus G_H [GPa]		5.93	6.13	3.64
Young's modulus Y_H [GPa]		14.03	14.62	9.23
Poisson ratio ν_H		0.18	0.19	0.26
Pugh's ratio B/G		1.24	1.29	1.81
Cauchy pressure $C_p = C_{12} - C_{44}$		−2.50	−2.34	0.52
Vicker hardness H_v		2.52	2.48	1.16
Kleinman parameter ξ		0.45	0.49	0.67
Anisotropy A		1.07	1.17	1.16
Melting temperature T_m [K]		641.35	643.72	618.23
Debye temperature θ_D [K]		110.20	124.82	91.61
Transverse velocity ν_t [m sec^{-1}]		1304.76	1410.09	1049.16
Longitudinal velocity ν_l [m sec^{-1}]		2095.74	2284.11	1861.32
Mean velocity ν_m [m sec^{-1}]		1437.92	1555.40	1167.14
Lame 1st constant λ		3.44	3.82	4.18
Lame 2nd constant μ		5.93	6.13	3.64
Grüensien parameter γ		2.57	2.55	2.28
Machinability μ_M		1.20	1.21	1.70
Thermal expansion α		2.70×10^{-4}	2.61×10^{-4}	4.39×10^{-4}

borderline ductile (1.81).[41] In terms of hardness, Cs_3GaI_6 has the highest Vickers hardness (H_V) (2.52 GPa), followed closely by K_3GaI_6 (2.48 GPa), while Rb_3GaI_6 shows a much lower value (1.16 GPa), suggesting it is significantly softer,[42] make it suitable for flexible solar cells. Solid materials' hardness and wear resistance were assessed using Chen *et al.*'s methodology:[43]

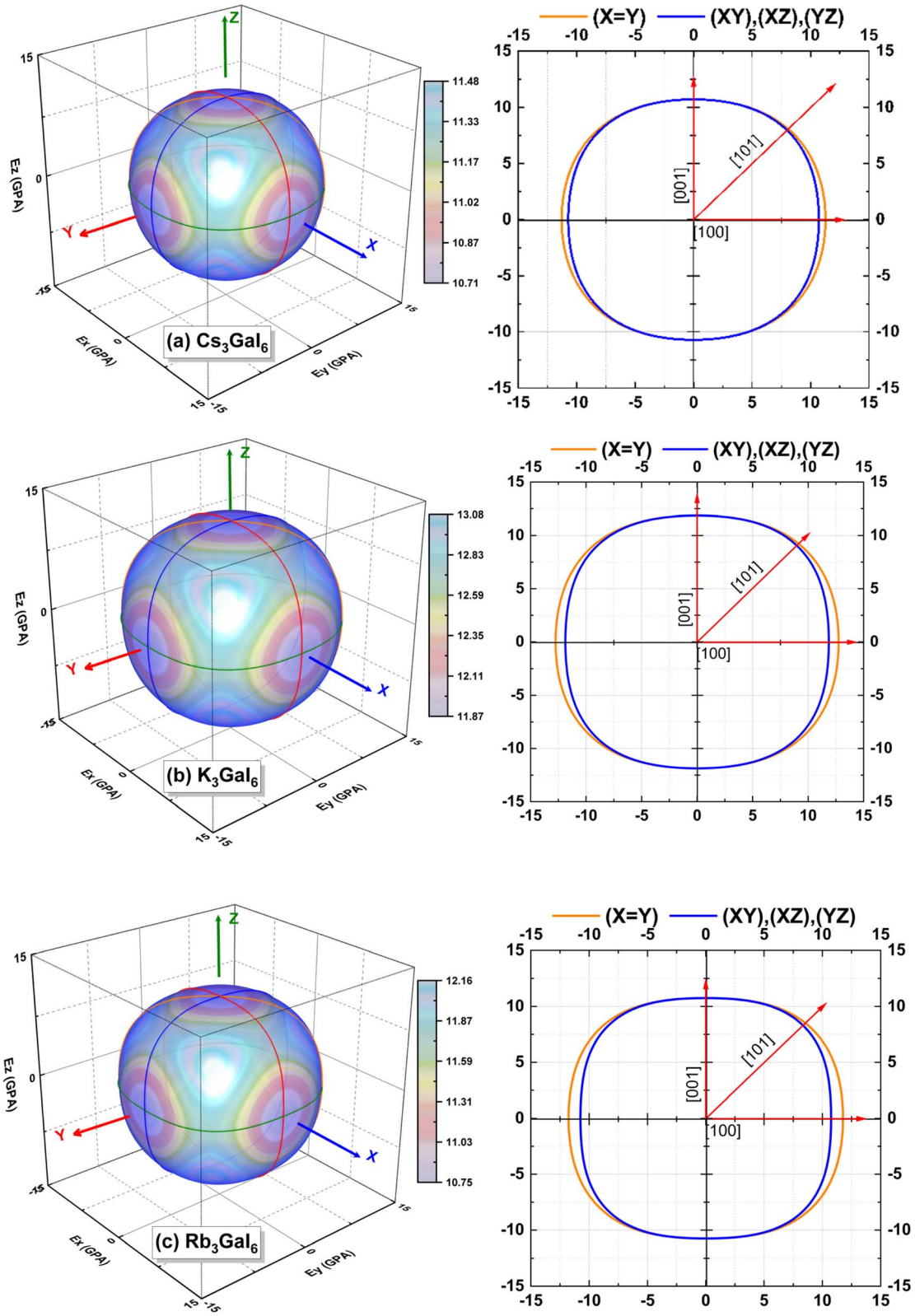

Fig. 4 3D and 2D projections of Young's modulus (in GPa) for (a) Cs_3GaI_6, (b) K_3GaI_6, and (c) Rb_3GaI_6.

$$H_V = 2\left(k^2 G_H\right)^{0.585} - 3,\ k = \frac{G_H}{B_H} \tag{10}$$

The Kleinman parameter (ξ) is useful for evaluating crystal stability against bond stretching and bending, it generally ranges from 0 to 1,[44] estimating *via* eqn (11).

$$\xi = \frac{C_{11} + 8C_{12}}{7C_{11} + 2C_{12}} \tag{11}$$

For the three compounds, the Kleinman parameter (ξ) is less than 1, signifying the highest mechanical stability and the strongest resistance to internal strain under deformation, where Cs_3GaI_6 exhibiting the lowest ξ at 0.45. The anisotropy factor (A), another crucial mechanical property, is slightly greater than 1 for all three compounds, indicating marginal elastic anisotropy that is nearer isotropy.[45] Determine the degree of elastic anisotropy in crystals using the two-dimensional (2D) and three-dimensional (3D) representations of crystal direction dependence of elastic moduli for a more thorough investigation of anisotropy.[46] The elastic modulus is isotropic when the 3D closed surface is perfectly spherical. If the closed surface is not a perfect sphere, on the other hand, this distortion shows the degree of anisotropy in the modulus of elasticity, indicating that the direction affects the elastic properties. The three-dimensional (3D) and two-dimensional (2D) representations of elastic anisotropy provide valuable insights into the directional dependence of mechanical properties in A_3GaI_6 (A = K, Rb, Cs) halide compounds as presented Fig. 4. These plots illustrate the variation of Young's modulus (Y_H) across different crystallographic directions, allowing for a deeper understanding of their mechanical stability and anisotropic nature. As reflected in the plots and quantified by the anisotropy index A, all three materials exhibit deviations from perfect isotropy. Cs_3GaI_6, with the lowest anisotropy index A = 1.07, shows the most isotropic elastic behavior, represented by a nearly spherical 3D surface, suggesting a uniform mechanical response in all directions (see Fig. 4(a)). As presented Fig. 4(b)–(c) Rb_3GaI_6 and K_3GaI_6, with slightly higher anisotropy indices of 1.16 and 1.17, respectively, exhibit more pronounced deviations from spherical symmetry, indicating increased directional dependence of their stiffness. These variations are primarily influenced by the size and bonding environment of the A-site cation, where the smaller K^+ and Rb^+ ions introduce subtle lattice distortions that enhance elastic anisotropy. Consequently, while Cs_3GaI_6 may offer more mechanically isotropic performance, Rb_3GaI_6 and K_3GaI_6 could be more sensitive to applied stress orientation. Understanding these anisotropic characteristics is crucial for selecting suitable A-site cations in designing materials for mechanically demanding or flexible optoelectronic applications.

A crucial measure of a material's thermal stability is its melting temperature, which is especially significant for photocatalytic systems that generate heat and are exposed to constant light. The estimated melting temperatures (T_m) are relatively close, 641.35 K (Cs_3GaI_6), 643 K (K_3GaI_6), 618 K (Rb_3GaI_6), consistent with their mechanical stability trends. This temperature is estimated by:[47]

$$T_m = 553 + 5.19C_{11} \pm 300 \tag{12}$$

Moreover, the Debye temperature (θ_D), a measure of lattice vibrational properties, is highest for K_3GaI_6 (124.82 K), reflecting its stronger interatomic forces, and lowest for Rb_3GaI_6 (91.61 K). The Debye temperature is determined by the average velocity of elastic waves (V_m), which is directly related to the natural frequency of vibrations in the elastic lattice.

$$\theta_D = \frac{h}{K_B}\left[\frac{3n}{4\pi V_a}\right]^{1/3} V_m \tag{13}$$

The calculated transverse (v_t), longitudinal (v_l), and mean (v_m) sound velocities show the same trends as the Debye temperature (θ_D), with K_3GaI_6 once again showing the highest values, making it the most acoustically stiff material.

$$V_m = \left[\frac{1}{3}\left(\frac{2}{{v_l}^2} + \frac{2}{{v_t}^3}\right)\right] - 1\Big/3,\ v_l = \left[\frac{3B_H + 4G_H}{3\rho}\right](1/2),\ \text{and}\ v_t = \left[\frac{G_H}{\rho}\right](1/2) \tag{14}$$

Additional crucial mechanical constants, Lame's coefficients are defined as $\lambda = C_{12}$ and $\mu = G_H$ for isotropic materials.[2] In light of this, the estimated values for Cs_3GaI_6 indicate that the requirements for isotropic molecules are closely satisfied. Furthermore, K_3GaI_6 and Cs_3GaI_6 have stronger mechanical robustness than Rb_3GaI_6, as indicated by their larger μ values (6.13 and 5.93 GPa, respectively) in the Lame constants (λ and μ). Lastly, the three have comparable values for the Grüneisen parameter (γ), which measures thermal anharmonicity and ranges from 2.28 to 2.57, indicating moderate lattice expansion and thermal conductivity. It is interesting to note that Rb_3GaI_6 has the largest thermal expansion coefficient ($\alpha = 4.39 \times 10^{-4}\ K^{-1}$) and machinability index ($\mu_M = 1.70$), suggesting that it may be simpler to process but may experience thermal instability. In summary, K_3GaI_6 emerges as the most mechanically robust, acoustically stiff, and thermally stable among the three, making it suitable for structural or high-frequency applications. Cs_3GaI_6 offers a good balance between hardness, thermal resistance, and covalent bonding character, while Rb_3GaI_6, though softer and more ductile, may be less favorable for applications requiring high mechanical integrity but might be interesting where machinability and processability are desired. Given its superior ductility and softer mechanical behavior, Rb_3GaI_6 is the most promising candidate for integration in flexible perovskite solar cells, where mechanical compliance and ease of processing are essential. However, this conclusion remains preliminary, as a comprehensive assessment requires further analysis of its electrical and optical properties, which will be discussed in the following sections.

3.2 Evaluation of the electronic properties of A_3GaI_6 (A = K, Rb, Cs)

The electronic band structures and corresponding total and partial densities of states (DOS) for A_3GaI_6 (A = K, Rb, Cs)

compounds, calculated using the TB-mBJ and TB-mBJ+SOC approaches, are presented in Fig. 5. All three halide double perovskites exhibit a direct band gap located at the L-symmetry point in the Brillouin zone. The calculated band gap values using TB-mBJ and TB-mBJ+SOC are 2.06/1.88 eV for Cs_3GaI_6, 1.94/1.76 eV for Rb_3GaI_6, and 1.83/1.65 eV for K_3GaI_6,

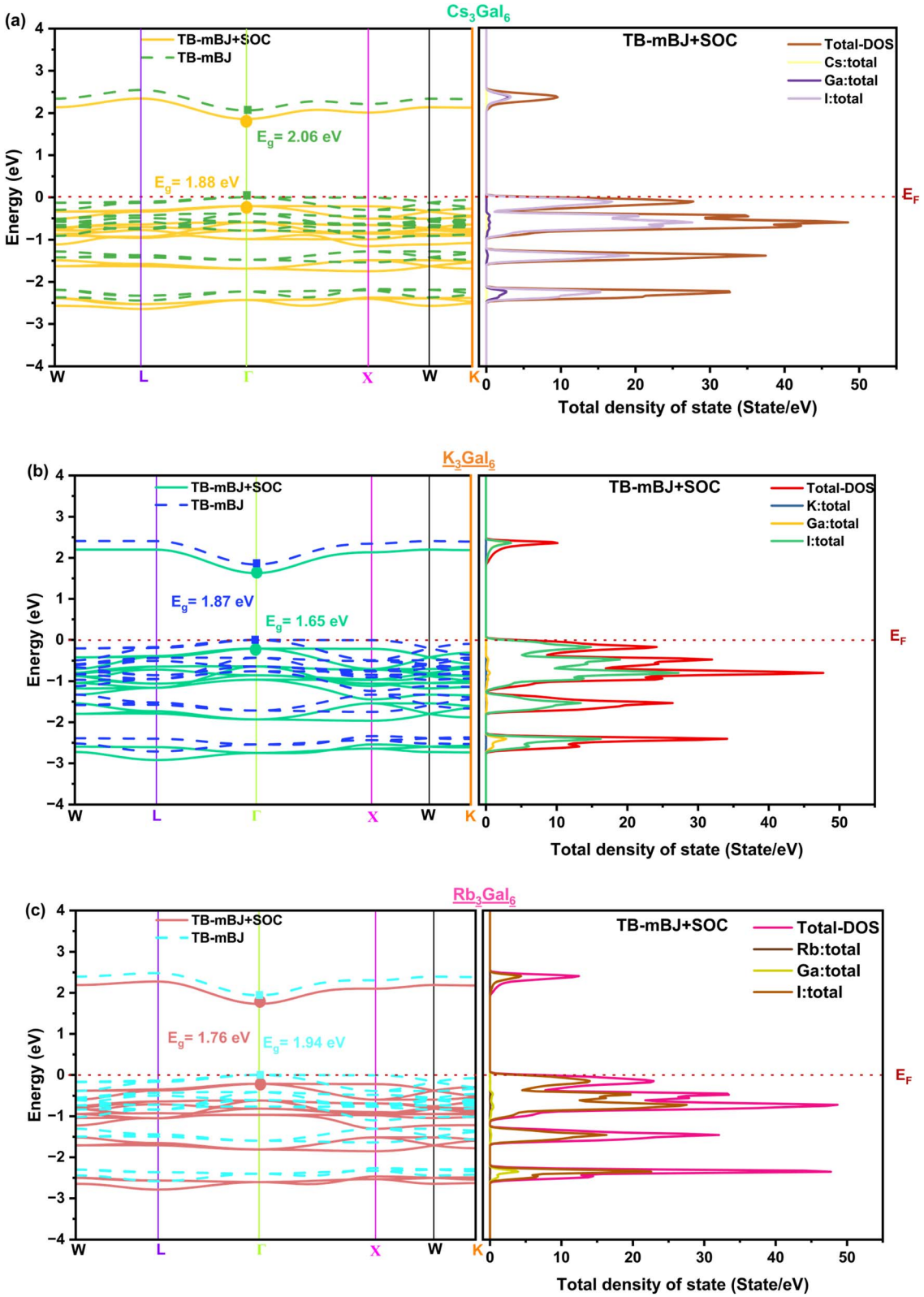

Fig. 5 Band structure is determined using the two methods TB-mBJ and TB-mB+SOC, whereas total density of state (TDOS) is determined using TB-mB+SOC, (a) Cs_3GaI_6, (b) K_3GaI_6, and (c) Rb_3GaI_6.

respectively. These values indicate strong absorption capabilities in the visible region, essential for photovoltaic applications. Notably, the inclusion of SOC slightly narrows the band gap for all compounds, reflecting relativistic effects predominantly due to the heavy iodine atoms. This consistent and direct E_g, falling within the visible spectrum, highlights the potential of K_3GaI_6 and Rb_3GaI_6 particularly when analyzed using TB-mBJ+SOC as suitable candidates for applications in solar cells. There is currently a dearth of experimental data on the bandgap values for A_3GaI_6 (A = Cs, K, and Rb) in the literature. This makes it more difficult to confirm theoretical predictions and prevents a thorough understanding of the electronic properties of these materials, especially for photovoltaic and optoelectronic applications. To validate computational results and evaluate these materials' potential for device integration, precise experimental measurements would be necessary. The TDOS of A_3GaI_6 (A = Cs, K, and Rb) is also shown in Fig. 5 using TB-mB+SOC. The Fermi level ($E_F = 0$) is chosen as the energy reference, and as shown here, the valence band maxima (VBM) and conduction band minima (CBM) are positioned at L symmetric *k*-points, respectively, resulting in a direct band gap. Furthermore, it appears that the E_F level is empty, suggesting that A_3GaI_6 (where A stands for Cs, K, and Rb) has a semiconducting nature. Despite slight variations, the band dispersions remain similar across the three materials, indicating comparable electronic transport properties. TDOS profiles further confirm that the valence and conduction band maximum is mainly composed of I and Ga states.

Additionally, the states in the highest valence band are flat along the (*L*-Γ-*X*) path in both band structure with and without SOC approach, confirming the low occupied orbital near E_F, this can be linked to the effective mass of the relatively large holes. Nevertheless, using both approaches (with and without SOC), the conduction band showed a dispersion, indicating n-type conductivity.[48] In other hand, in the partial density of states (PDOS) of A_3GaI_6 (A = K, Rb, Cs), shown in Fig. 6, highlights the atomic orbital contributions to the electronic structure. Across all three compounds, the valence band (−4 eV to 0 eV) is primarily governed by I–p and I–Ga states, confirming the strong I–Ga bonding framework. The conduction band (above 0 eV) is mainly dominated by Ga–p states, with minor contributions from I–p orbitals, reflecting that Ga plays the central role in electronic transitions. The A-site cations (K, Rb, Cs) contribute only weakly to the electronic states near the band edges: Cs and Rb show faint but discernible features close to the VBM, while K exhibits nearly negligible involvement due to minimal orbital overlap.[49] This highlights that the A-site cations primarily act as structural stabilizers rather than direct contributors to the frontier states at the VBM or CBM. Instead, their main role lies in tuning the crystal structure and electrostatics. Variation in cation (Cs, K, and Rb) size alters the lattice constant, octahedral tilts, and Ga–I bond lengths/angles, effectively applying a "chemical pressure" that modulates I–p/Ga–p hybridization and bandwidths.[50] In addition, changes in cell volume impact dielectric screening and spin–orbit coupling corrections (TB-mBJ *vs.* TB-mBJ+SOC), further renormalizing the band gap. Following the ionic size trend ($K^+ < Rb^+ < Cs^+$), K_3GaI_6 undergoes the strongest chemical pressure, leading to shorter Ga–I bonds, broader bandwidths, and hence the smallest gap; Rb_3GaI_6 shows intermediate behavior; while Cs_3GaI_6, with the largest lattice and weakest distortions, exhibits the widest gap.

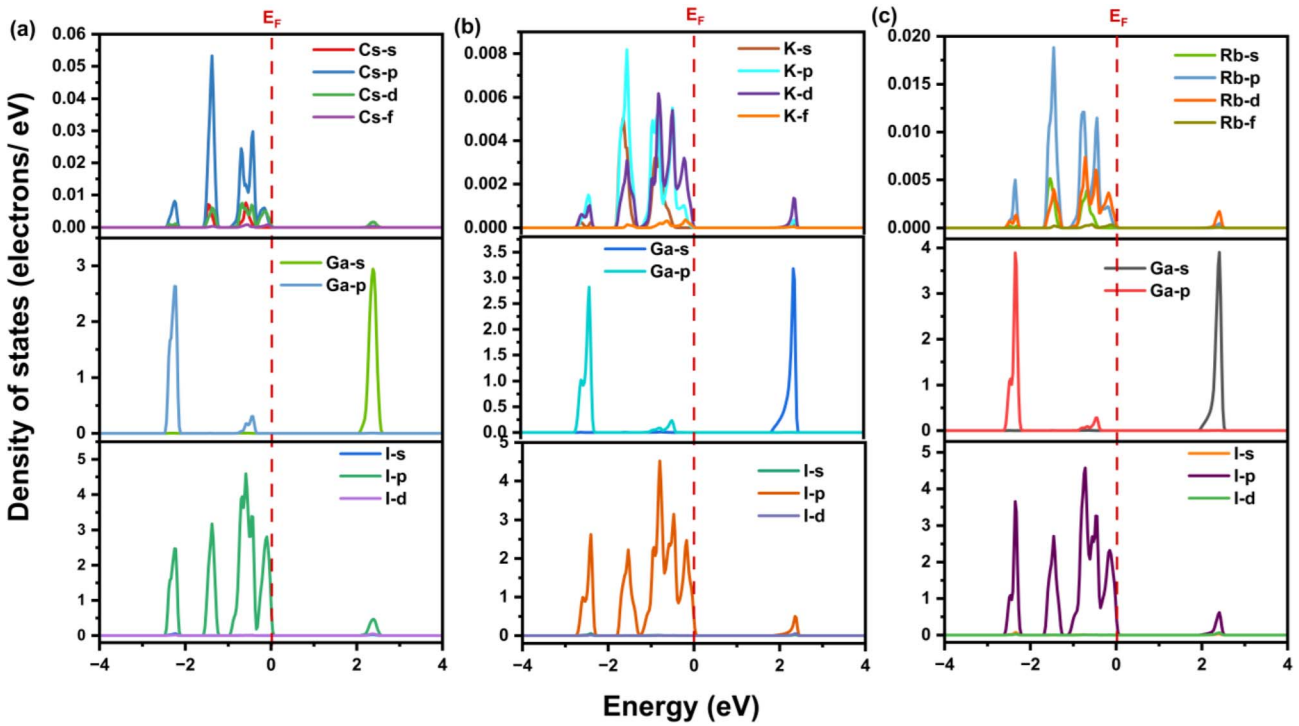

Fig. 6 The partial density of states (PDOS) for (a) Cs_3GaI_6, (b) K_3GaI_6, and (c) Rb_3GaI_6.

Table 3 Carrier density ($\times 10^{15}$ cm^{-2}) of A_3GaI_6 halide perovskites

Compounds	K-4s	Rb-5s	Cs-6s	Ga-4s4p	I-5s	I-5p	Total
K_3GaI_6	0.344	—	—	0.022	0.053	0.124	0.543
Rb_3GaI_6	—	0.110	—	0.298	0.00027	0.175	0.583
Cs_3GaI_6	—	—	0.153	0.0595	0.0528	0.092	0.357

To gain deeper insight into the electronic behavior and bonding nature of A_3GaI_6 (A = Cs, K, and Rb), the orbital-resolved carrier density and Bader charge analysis were investigated. The orbital carrier density provides information about the atomic and orbital contributions at the band edges, which is essential for understanding the origin of charge transport and optical transitions. Table 3 summarizes the findings, which indicate that the A-site cations (K, Rb, Cs) make a substantial contribution to the carrier density. The K-4s orbitals in K3GaI6 exhibit the highest ρ value of 0.344×10^{15} cm^{-2}, followed by Rb-5s in Rb_3GaI_6 (0.110×10^{15} cm^{-2}) and Cs-6s in Cs_3GaI_6 (0.153×10^{15} cm^{-2}). We have observed moderate contributions to the Ga-4s4p orbitals for K_3GaI_6, Rb_3GaI_6, and Cs_3GaI_6: 0.022×10^{15} cm^{-2}, 0.298×10^{15} cm^{-2}, and 0.0595×10^{15} cm^{-2}. It is intriguing that the Iodine orbitals (I-5s and I-5p) make a substantial contribution to the total carrier density, particularly in Rb_3GaI_6 (I-5p: 0.175×10^{15} cm^{-2}) and K_3GaI_6 (I-5p: 0.124×10^{15} cm^{-2}). In contrast, Cs_3GaI_6 exhibits a more balanced distribution (I-5s: 0.0528, I-5p: 0.092×10^{15} cm^{-2}). The total carrier densities of these perovskites are on the order of 10^{15} cm^{-2}: K_3GaI_6 (0.543×10^{15} cm^{-2}), Rb_3GaI_6 (0.583×10^{15} cm^{-2}), and Cs_3GaI_6 (0.357×10^{15} cm^{-2}). This magnitude is comparable to certain high-carrier-density Janus MXenes materials, such as Sc_2CFCl ($\sim 4 \times 10^{15}$ cm^{-2}), and is substantially larger than typical semiconductors. This suggests that these halide perovskites could facilitate efficient charge transport.[34] It is intriguing that K_3GaI_6 demonstrates the highest contribution from the A-site cation, whereas Rb_3GaI_6 exhibits the highest Ga and I contributions. These findings suggest that the electronic distribution is susceptible to subtle changes as a result of the cation's size and electronegativity. The lowest total carrier density is observed in Cs_3GaI_6, which contains the heaviest A-site cation. This trend indicates that lighter alkali metals result in a greater contribution from the A-site s orbitals.

In parallel, the Bader charge (ΔQ) analysis quantifies the charge transfer between atoms and reveals the ionic or covalent character of the chemical bonding.[51] In Table 4, the results are summarized. It is evident that the A-site cations (K, Rb, Cs) have positive ΔQ values, which suggests that these electropositive metals donate electrons to the more electronegative elements in the lattice. K in K_3GaI_6 exhibits the largest positive charge (+0.85 e), succeeded by Rb in Rb_3GaI_6 (+0.60 e) and Cs in Cs_3GaI_6 (+0.50 e). This trend indicates a diminishing electron-donating capacity as the cation size escalates down the alkali group.[52] The moderate electron donation to the surrounding iodine atoms is indicated by the modest positive charges of the Ga atoms (+0.15, +0.20, and +0.10 e for K-, Rb-, and Cs-based perovskites, respectively). In contrast, the iodine atoms are primarily negative charged in their 5p orbitals (−0.45 e for K_3GaI_6 and Rb_3GaI_6; −0.35 e for Cs_3GaI_6), with a minimal contribution from their 5 s orbitals. This suggests that the iodide ions serve as the principal electron acceptors, accepting electrons from both A-site cations and Ga atoms. Interestingly, the total charge transfer appears to be largest in Rb_3GaI_6 (combined ΔQ magnitude), due to a balance of moderate electron donation from Rb and relatively strong transfer to I-5p orbitals. K_3GaI_6 shows a similar pattern, with most electrons localized on the K cations, while Cs_3GaI_6 exhibits lower overall charge transfer, consistent with its smaller carrier density observed in PDOS analysis.

Furthermore, another essential metric in solid-state physics derived from band structure is the effective mass, as it directly indicates the ease with which charge carriers (electrons or holes) can react to external forces within the crystal lattice. The valence band (VB) close to the Fermi level has little dispersion, according to band structure analysis, suggesting a comparatively large effective mass for hole carriers. In contrast, the conduction band (CB) is more dispersive, indicating that electrons possess a smaller effective mass (m_e^*). A smaller effective mass allows carriers to move more freely, resulting in higher mobility and improved electrical conductivity, conversely, a larger effective mass restricts carrier motion, reducing mobility and potentially limiting device performance, confirming the n-type nature of those semi-conductors.[53] Thus, the balance between electron and hole effective masses plays a decisive role in determining the transport properties and overall efficiency of semiconducting materials. Eqn (15) is used to determine the effective masses for hole carriers (m_h^*) and electrons (m_e^*) (see Table 5).

Table 4 Bader charges (ΔQ, in e) of atoms for A_3GaI_6 halide perovskites

Materials	A (K/Rb/Cs)	Ga	I-5s	I-5p
K_3GaI_6	+0.85	+0.15	−0.05	−0.45
Rb_3GaI_6	+0.60	+0.20	−0.02	−0.45
Cs_3GaI_6	+0.50	+0.10	−0.03	−0.35

Table 5 Summary of calculated parameters

Compound	m_e^*	m_h^*	μ_e (cm^2 V^{-1} s)	μ_h (cm^2 V^{-1} s)	N_C (cm^{-3})	N_V (cm^{-3})	N_A (cm^{-3})	N_D (cm^{-3})	$\varepsilon_1(0)$	$\eta(0)$	$R(0)$
Cs_3GaI_6	0.040	1.603	440	11	2.01×10^{17}	5.09×10^{19}	—	4.07×10^{10}	2.97	1.72	7.06
K_3GaI_6	0.036	0.548	488	32	1.71×10^{17}	1.02×10^{19}	—	1.55×10^{11}	3.13	1.76	7.71
Rb_3GaI_6	0.037	5.828	475	3	1.77×10^{17}	3.53×10^{20}	—	3.22×10^{11}	2.99	1.73	7.16

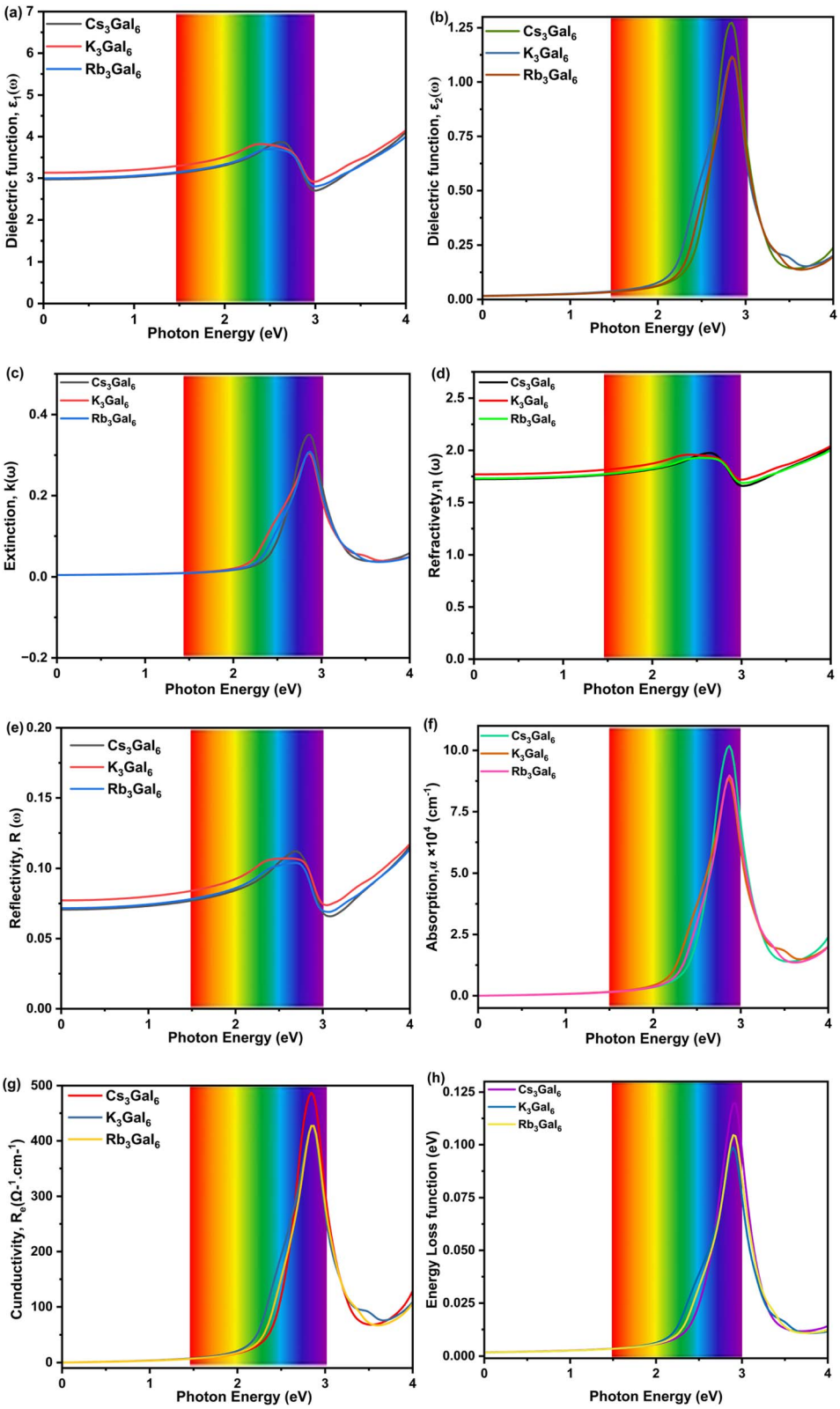

Fig. 7 A_3GaI_6 (A = Cs, K, and Rb)-based single halide perovskite compounds have the following computed optical properties: (a) and (b) dielectric functions, (c) extinction coefficient, (d) refractive index, (e) reflectivity, (f) absorption coefficient, (g) conductivity, and (h) loss function.

$$m^* = \hbar^2 \times \left(\frac{\partial^2 E(k)}{\partial k^2}\right)^{-1} \quad (15)$$

where $m^*(k)$, $\hbar$, $E(k)$ and k are the effective mass, reduced Plank's constant, energy and wave vector, respectively.

The importance of carrier mobility lies in its decisive role in governing charge transport within perovskite solar cells. In SCAPS-1D simulations, mobility (μ) is a key parameter because it determines how efficiently photogenerated electrons and holes can be extracted to the contacts. A higher mobility enhances drift-diffusion transport, minimizes recombination losses, and directly improves photovoltaic performance. Conversely, low mobilities limit carrier extraction even in materials with strong light absorption, resulting in reduced device efficiency. In similar perovskite compounds, electron and hole relaxation times (τ) are typically on the order of 10^{-12} s.[54,55] However, for A_3GaI_6 (A = Cs, K, and Rb), our optical analysis suggests much shorter relaxation times, around 10^{-14} s, which significantly limits carrier lifetimes, with q is elementary chare.

$$\mu = \frac{q\tau}{m^*} \quad (16)$$

The effective density of states in the conduction band (N_C) and valence band (N_V), which show the number of accessible states per unit volume at the band borders, is then influenced by the mass effective. These parameters are also very important in SCAPS-1D, they are supplied by:

$$N_c = 2\left(\frac{2\pi m_e^* k_B T}{h^2}\right)^{3/2}$$
$$N_v = 2\left(\frac{2\pi m_h^* k_B T}{h^2}\right)^{3/2} \quad (17)$$

where T stands for temperature, Boltzmann's constant, and Plank's constant. Table 3 provides a summary of all computed values for A_3GaI_6 (where A = Cs, K, and Rb) for comparison.

Additionally, the shallow donor density (N_D) and acceptor density (N_A) are two of the most important input parameters in SCAPS-1D since they directly affect the concentration of the majority of carriers in each layer, which in turn controls the simulated solar cell's built-in potential, depletion width, and current–voltage behavior. If shallow, fully ionized dopants are assumed, one can estimate N_D or N_A using the effective density of states (N_c and N_v) taken together. These values are listed in Table 5.

3.3 Evaluation of the optical properties of A_3GaI_6 (A = K, Rb, Cs)

The material's optical characteristics are influenced by electromagnetic waves, which also affect electrical and optical performance. The complex dielectric function $\varepsilon(\omega)$ in relation to angular frequency is able to be stated as follows:

$$\varepsilon(\omega) = \varepsilon_1(\omega) + i\varepsilon_2(\omega) \quad (18)$$

The real component $\varepsilon_1(\omega)$, is related to the refractive index and controls refraction, reflection, and light speed. It suggests that the material may retain energy as electric dipoles when exposed to an external electric field. Moreover, the imaginary part $\varepsilon_2(\omega)$ affects the absorption coefficient and, consequently, the amount of light absorption at frequencies. The values of the loss function, $L(\omega)$, reflectivity, $R(\omega)$, conductivity, $\sigma(\omega)$, refractive index, $\eta(\omega)$, extinction coefficient, $k(\omega)$, and absorption coefficient, $\alpha(\omega)$, were computed using eqn (18):

$$\eta(\omega) = \left(\sqrt{(\varepsilon_1{}^2(\omega) + \varepsilon_2{}^2(\omega))} + \varepsilon_1(\omega)\right)^{1/2} \Big/ \sqrt{2} \quad (19)$$

$$k(\omega) = \left(\sqrt{(\varepsilon_1{}^2(\omega) + \varepsilon_2{}^2(\omega))} - \varepsilon_1(\omega)\right)^{1/2} \Big/ \sqrt{2} \quad (20)$$

$$R(\omega) = \left|\frac{\varepsilon(\omega)^{1/2} - 1}{\varepsilon(\omega)^{1/2} + 1}\right|^2 \quad (21)$$

$$\alpha(\omega) = \sqrt{2\omega}\left(\sqrt{(\varepsilon_1{}^2(\omega) + \varepsilon_2{}^2(\omega))} - \varepsilon_1(\omega)\right)^{1/2} \quad (22)$$

$$\sigma(\omega) = \frac{-i\omega\varepsilon(\omega)}{4\pi} \quad (23)$$

$$L(\omega) = \frac{\varepsilon_2(\omega)}{\varepsilon_1{}^2(\omega) + \varepsilon_2{}^2(\omega)} \quad (24)$$

As shown Fig. 7(a), the static dielectric constant $\varepsilon_1(0)$ follows the order K_3GaI_6 (3.13) > Rb_3GaI_6 (2.99) > Cs_3GaI_6 (2.97), reflecting stronger polarizability and screening in the K-based compound. This trend is mirrored in the extinction coefficient near the absorption edge, where K3GaI6 exhibits a sharper onset of optical transitions.[56] The refractive index $n(0)$ similarly decreases slightly from 1.76 (K_3GaI_6) to 1.73 (Rb_3GaI_6) and 1.72 (Cs_3GaI_6), confirming the stronger optical confinement in K-based systems (see Fig. 7(d)). In contrast, the imaginary part $\varepsilon_2(\omega)$ as shown Fig. 7 (b), which originates from interband transitions, is most pronounced in Cs_3GaI_6, followed by Rb_3GaI_6 and K_3GaI_6, indicating stronger optical transitions and enhanced light–matter interaction in the Cs-based system.[57] This trend is mirrored in the extinction coefficient $k(\omega)$, where Cs_3GaI_6 exhibits the largest peak values, confirming its stronger absorption capability (see Fig. 7(c)). Additionally, all compounds exhibit absorption coefficients greater than 10^5 cm^{-1} as presented in Fig. 7(f), with Cs3GaI6 showing the highest values, making it particularly promising for photovoltaic applications by ensuring efficient light harvesting.[58] At the same time, the reflectivity remains low (see Fig. 7(e)), decreasing from 7.71% (K_3GaI_6) to 7.16% (Rb_3GaI_6) and 7.06% (Cs_3GaI_6), which minimizes surface photon losses. This low reflectivity, combined with the highest absorption in Cs_3GaI_6, further enhances its suitability for solar energy conversion. The optical conductivity spectra (see Fig. 7(g)) further confirm efficient carrier generation in the visible range, consistent with the absorption behavior, where Cs_3GaI_6 exhibits the highest optical conductivity, in agreement with its superior absorption coefficient. Finally, the energy loss function as shown in Fig. 7(h),

identifies pronounced plasmon peaks, indicating strong collective oscillations of charge carriers that play a key role in screening and charge transport.[59]

Among the investigated A_3GaI_6 (A = K, Rb, Cs) compounds, all exhibit direct band gaps within the visible region together with high absorption coefficients, indicating their potential as photovoltaic absorbers. However, the choice of the most suitable material cannot rely only on the band-gap value alone and must consider the transport and dielectric properties that directly affect device performance. In this context, K_3GaI_6 presents the most favorable optoelectronic profile, with a band gap of 1.65 eV (TB-mBJ+SOC), which is closest to the optimal range for single-junction solar cells and enables more efficient solar-spectrum utilization. Moreover, its lower carrier effective masses and higher electron and hole mobilities indicate more efficient charge transport, while its larger static dielectric constant suggests stronger dielectric screening and improved separation of photogenerated carriers. These combined features make K_3GaI_6 the most suitable candidate for device-level investigation, whereas the wider band gaps and less favorable transport parameters of Cs_3GaI_6 and Rb_3GaI_6 would limit their photocurrent generation and carrier extraction under identical conditions. From a mechanical point of view, K_3GaI_6 is classified as brittle according to the Pugh ratio and Cauchy pressure; nevertheless, this does not restrict its applicability in photovoltaic devices. Solar-cell absorbers are generally employed as thin films deposited on mechanically robust substrates and encapsulated within multilayer architectures, where the active layer is not subjected to significant mechanical stress. Consequently, ductility is not a prerequisite for photovoltaic operation, as demonstrated by widely used brittle semiconductors such as crystalline Si and III–V compounds. Based on these considerations, K_3GaI_6 is selected as the absorber for the subsequent SCAPS-1D device simulations.

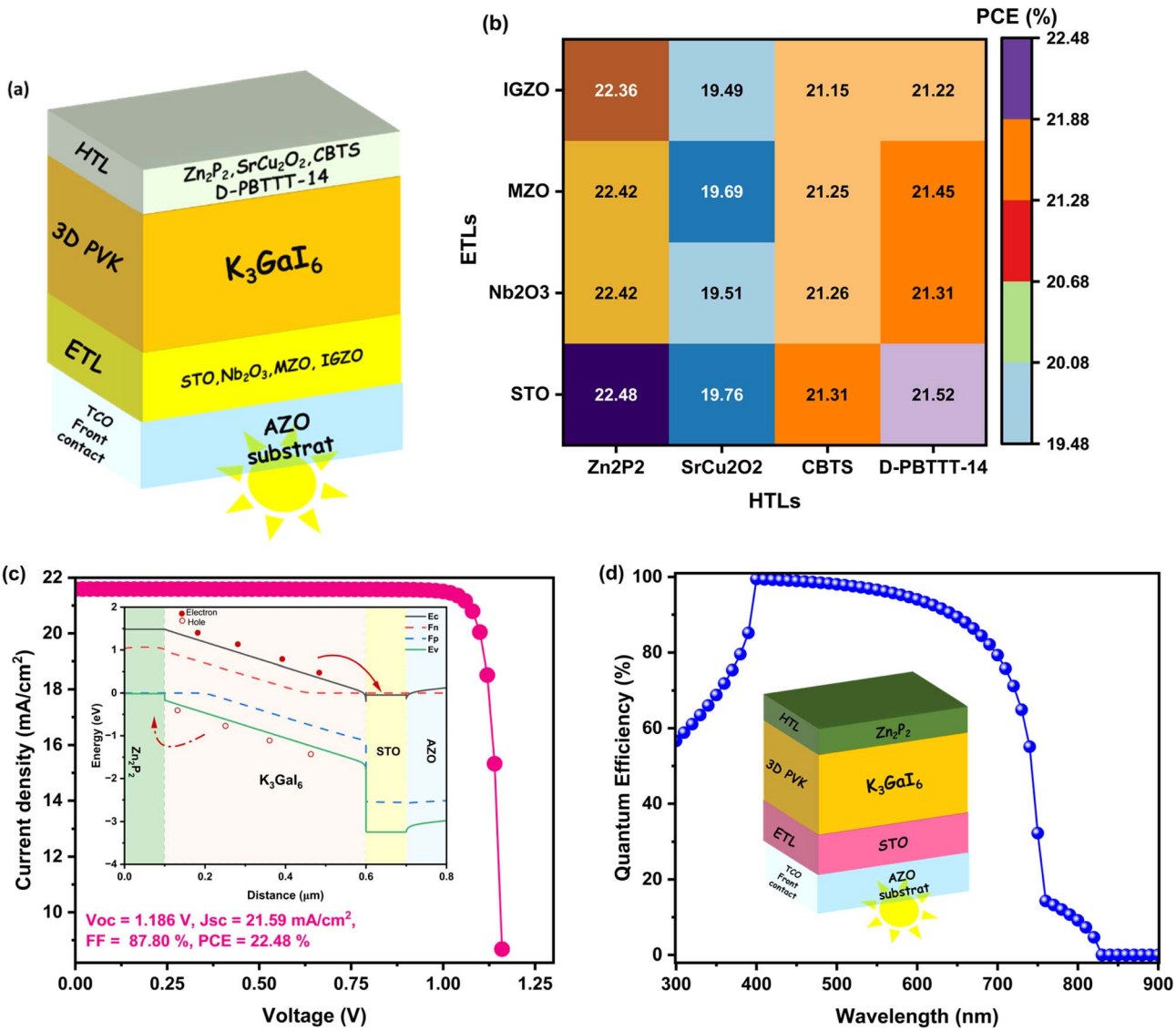

Fig. 8 (a) Schematic of structure of K_3GaI_6-based PSC with different HTLs and ETLs, (b) heatmap of PCE for 16 configurations, (c) *I–V* curve of the best device (AZO/STO/K_3GaI_6/Zn_2P_2), with inset presented its band diagram, (d) quantum efficiency of the best device with its structure in the inset.

Table 6 Inputs used in SCAPS-1D for all layers

	TCO	PVK	HTLs			ETLs				
Parameters	AZO	K_3GaI_6	$SrCu_2O_2$	Zn_3P_2	CBTS	D-PBTTT-14	MZO	STO	IGZO	Nb_2O_5
Thickness (nm)	100	500	100	100	100	100	100	100	100	100
E_g (eV)	3.10	1.650	3.3	1.5	1.5	2.16	3.35	3.2	3.05	3.4
χ (eV)	4.1	4.200	2.2	4.2	4.22	3.2	4	4	4.16	3.9
ε_r	9.00	3.350	9.77	7.11	5.5	10	66	8.7	10	10
N_c (cm^{-3})	1.1×10^{17}	1.71×10^{17}	2×10^{20}	2.2×10^{18}	2.20×10^{18}	2.8×10^{19}	1×10^{19}	1.7×10^{19}	5×10^{18}	2.20×10^{18}
N_v (cm^{-3})	1.0×10^{18}	1.02×10^{17}	2×10^{21}	1.8×10^{19}	1.80×10^{19}	1.0×10^{19}	1×10^{19}	2×10^{20}	5×10^{18}	1.8×10^{19}
μ_n ($cm^2\ V^{-1}\ s^{-1}$)	100	488	0.1	3.8	5.00	2.83×10^{-3}	0.05	5.3×10^{3}	15	20
μ_p ($cm^2\ V^{-1}\ s^{-1}$)	25	32	0.46	1	1.50	2.83×10^{-3}	0.05	6.6×10^{2}	0.2	0.1
N_D (cm^{-3})	1.0×10^{15}	1.55×10^{11}	0	0	0	0	1×10^{17}	2×10^{16}	1×10^{17}	1.00×10^{16}
N_A (cm^{-3})	0	0	1.0×10^{17}	1.0×10^{19}	1.00×10^{18}	1×10^{18}	0	0	0	0
N_t (cm^{-3})	1.0×10^{14}	Varied	1.0×10^{14}	1.0×10^{14}	1.00×10^{14}	1×10^{14}	1×10^{14}	1×10^{14}	1×10^{15}	1.00×10^{15}
References	60	DFT	61	62	63	64	65	66	67	68

3.4 Design and simulation of K_3GaI_6-Based single-halide perovskite solar cells

Based on DFT-derived parameters, an n-i-p device structure (AZO/ETLs/K_3GaI_6/HTLs) was modeled in SCAPS-1D to bridge material-level insights with device-level performance (see Fig. 8(a)). K_3GaI_6 was selected as the absorber due to its optimal band gap within the visible range, balanced optical absorption, and favorable electronic properties, which together indicate

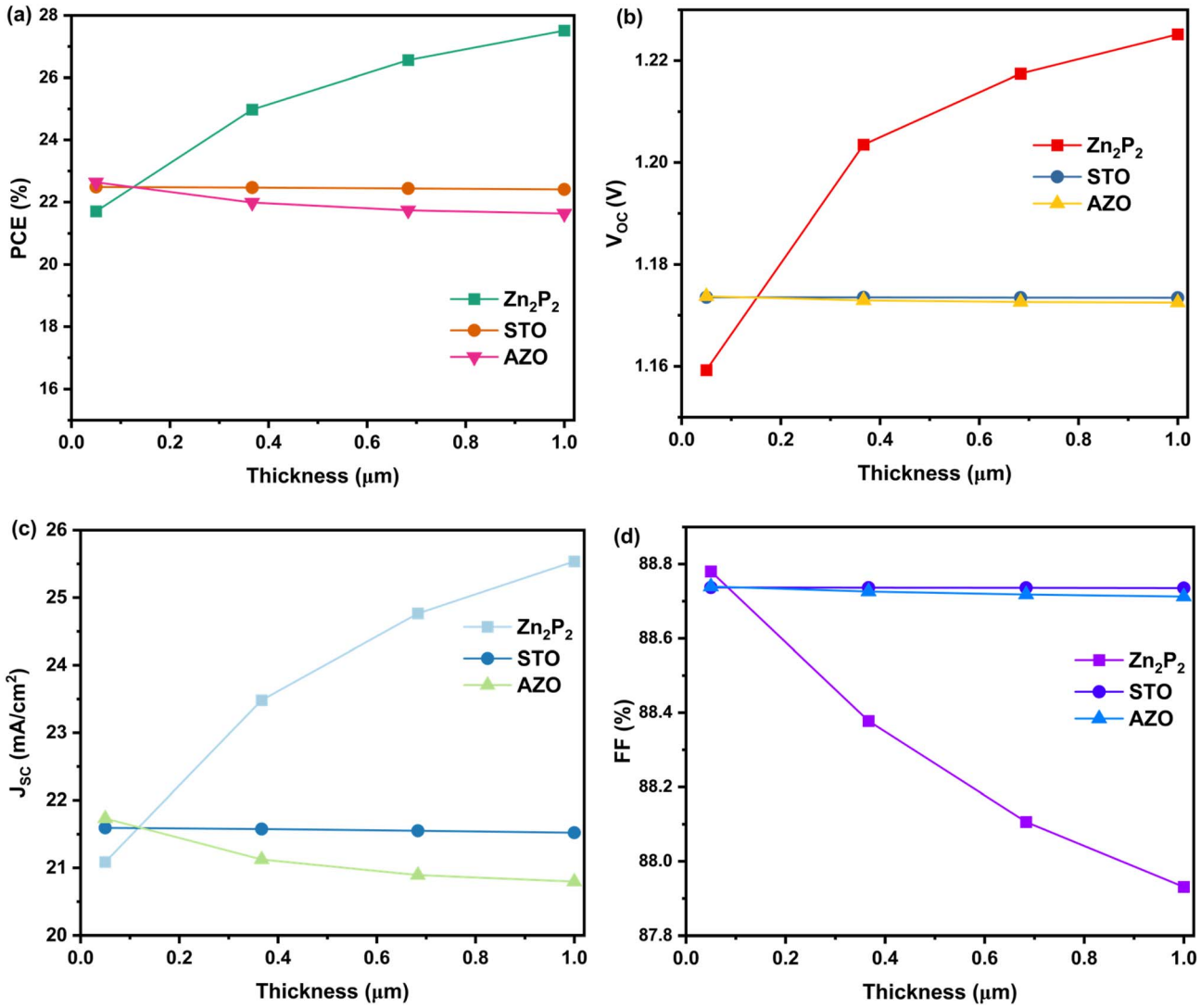

Fig. 9 Photovoltaic parameters of AZO/STO/K_3GaI_6/Zn_3P_2 under variation of thickness of layers, (a) PCE, (b) V_{OC}, (c) J_{SC}, and (d) FF.

strong potential for photovoltaic applications. The integration of DFT-derived parameters into SCAPS-1D simulations provides a powerful framework for determining the most efficient and stable device configurations. Using these inputs (summarized in Table 6), we systematically screened a series of 16 K_3GaI_6-based solar cell architectures. The performance outcomes, illustrated as a heatmap in Fig. 8(b), highlight the variation in PCE across different configurations. For this comparative study, the thicknesses of the ETL, HTL, and TCO layers were fixed at 500 nm, while the perovskite absorber (K_3GaI_6) was also set to 500 nm, ensuring consistency in evaluating the structural variations and identifying the optimal architecture. The devices AZO/ETLs/K_3GaI_6/Zn_2P_2 have the greatest PCE of all those configurations, at about 22%. Of those structures, AZO/STO/K_3GaI_6/Zn_2P_2 has the highest PCE of 22.5%, V_{OC} of 1.186 V, J_{SC} of 21.59 mA cm^{-2} and FF of 87.80% (see Fig. 8(c)), demonstrating the combination's outstanding performance. It is possible that the suitable affinity of PVK, ETL, and HTL, which enables the transfer of charge from PVK (K_3GaI_6) to STO (ETL) and Zn_2P_2 (HTL), as illustrated by band diagram in inset of Fig. 8(c), explains these photovoltaics characteristics, which might be regarded as promising results for future environmentally friendly perovskite devices.

For the K_3GaI_6-based perovskite solar cell, the quantum efficiency (QE) curve exhibits a high response in the visible spectrum as presented in Fig. 8(d), peaking between roughly 400 and 600 nm, indicating effective photon absorption and charge carrier extraction in this range.[69] The QE steadily decreases between 750 and 800 nm after 600 nm, indicating that absorption is constrained by the material's bandgap. It is anticipated that perovskite materials with moderate bandgaps will exhibit a low response in the near-infrared range (above 800 nm). The general pattern indicates that although the device performs well in the visible spectrum, more modification would be required to optimize near-infrared absorption and carrier transmission.

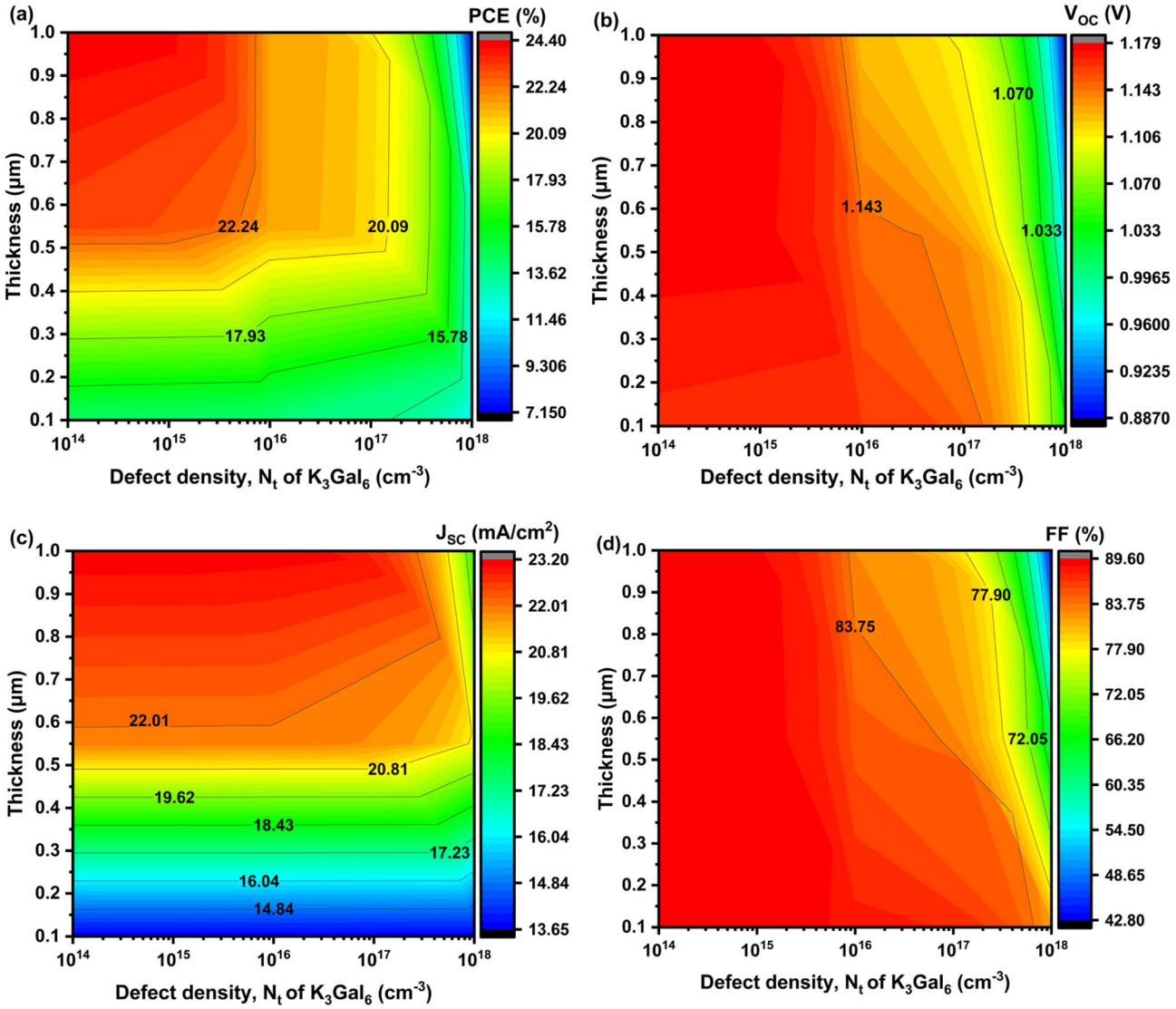

Fig. 10 AZO/STO/K_3GaI_6/Zn_2P_2 heat contour under varying thickness and defect density of K_3GaI_6 PVK (a) PCE, (b) V_{OC}, (c) J_{SC}, and (d) FF.

In this section, we examine the influence of the HTL, ETL, and TCO thicknesses on the photovoltaic performance of K_3GaI_6-based PSCs. The thicknesses of Zn_2P_2 (HTL), STO (ETL), and AZO (TCO) were varied from 0.05 to 1 μm, as shown in Fig. 9. The results indicate a generally positive effect of thickness on all photovoltaic parameters, except for FF, which shows only a negligible variation (from 87% to 88%). Interestingly, this slight improvement is observed only in the HTL (Zn_2P_2), while the ETL (STO) and TCO (AZO) have almost no influence on the device performance. This behavior suggests that optimizing the HTL thickness can slightly enhance charge extraction and reduce interfacial recombination, whereas increasing the ETL and TCO thicknesses mainly affects series resistance without significantly contributing to efficiency.

On the other hand, the absorber layer represents the most critical component of a photovoltaic solar cell, as it is directly responsible for light absorption and charge generation. To evaluate its influence, we varied both the thickness and defect density (N_t) of the K_3GaI_6 absorber. The thickness was altered from 0.1 to 1 μm, while N_t was tuned from 10^{14} to 10^{18} cm^{-3}. As shown in the contour mapping of Fig. 10, the optimal photovoltaic parameters are obtained at a thickness of 1 μm combined with the lowest defect density (10^{14} cm^{-3}). Two key points are highlighted by this trend: maintaining a low defect density is essential for minimizing non-radiative recombination, which directly supports higher V_{OC} and FF, and increasing absorber thickness improves light harvesting and photocurrent generation, which leads to improved J_{SC} and overall PCE.[70] Despite the advantages of thickness, trap-assisted recombination takes over at larger defect densities, significantly decreasing device efficiency. These findings highlight how crucial it is to properly develop the absorber's thickness and material quality in order to attain the best possible device performance.

In the previous section, we focused on identifying the optimal structural parameters that could enhance the photovoltaic performance of the K_3GaI_6-based device. Taking these findings into account, we observed that the lowest thickness of STO (ETL) and AZO (TCO) at 0.05 μm, combined with a moderate thickness of 0.5 μm for Zn_2P_2 (HTL), provided

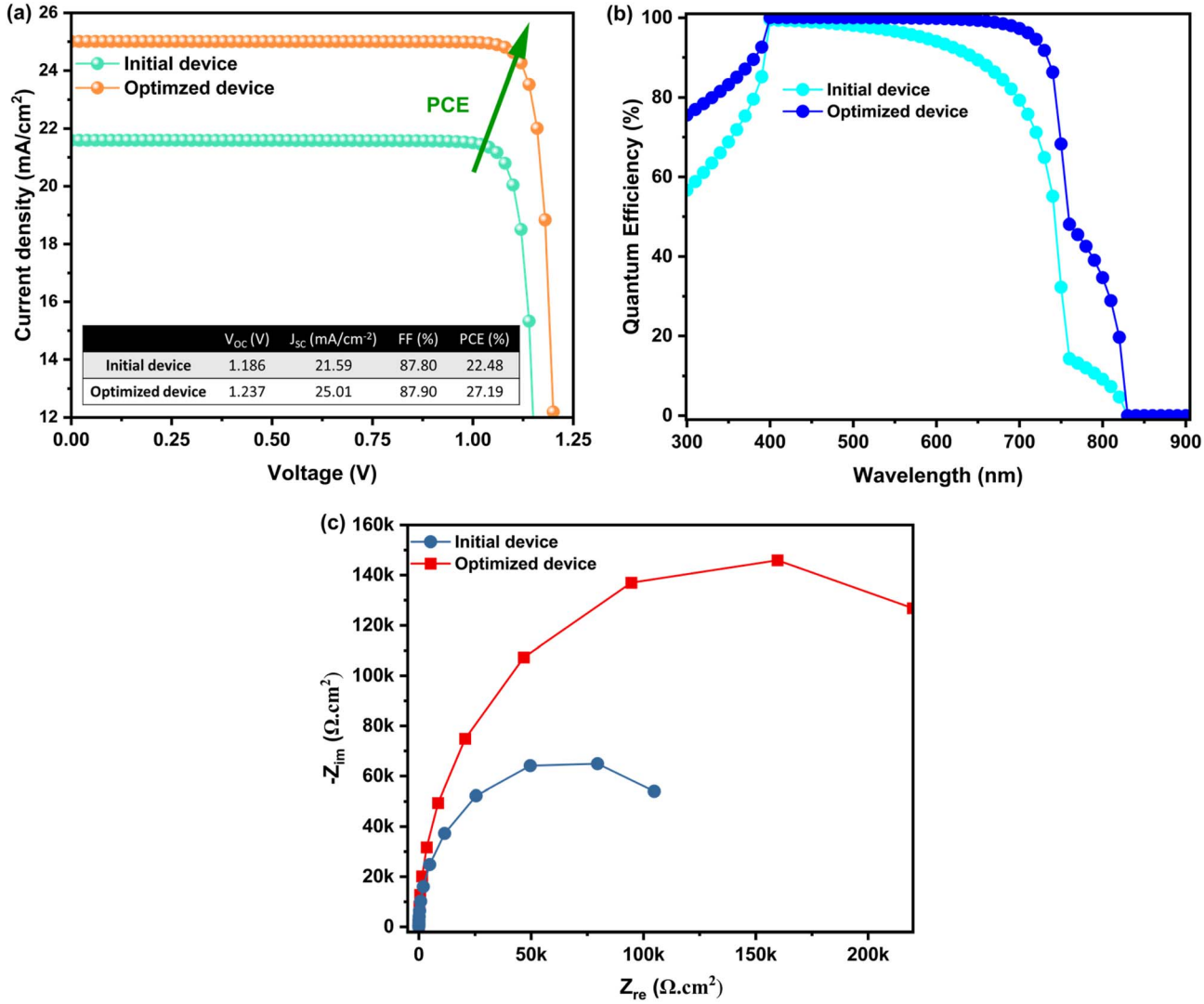

Fig. 11 A comparison between initial and optimized device by (a) *I*–*V* curve, (b) QE, and (c) Nyquist plots of initial and optimized device.

favorable conditions for efficient charge extraction and transport. At the same time, the absorber (K_3GaI_6) achieved its best performance at a thickness of 1 μm with a low defect density of 10^{14} cm^{-3}. Together, these optimized parameters resulted in a significant enhancement of the overall device performance, demonstrating the critical balance between layer thicknesses and defect passivation for maximizing efficiency. Through systematic optimization, the K_3GaI_6-based device demonstrated a remarkable performance improvement, with the PCE rising from 22.48% to 27.19%, approaching the Shockley–Queisser limit of 33%,[71] as shown in the *J–V* curve (Fig. 11(a)). The inset table of this figure further confirms that not only PCE but also the other photovoltaic parameters were enhanced: V_{OC} increased from 1.186 to 1.237 V, J_{SC} from 21.59 to 25.01 mA cm^{-2}, and FF from 87.80% to 87.90%. In addition, QE spectrum of the optimized device shows clear enhancement across the entire visible range (400–700 nm), as illustrated in Fig. 11(b). Equally important, the Nyquist plots (Fig. 11(c)) reveal a substantial expansion of the semicircle diameter for the optimized device compared to the original one. This enlargement is a hallmark of higher charge-transfer resistance at the perovskite/HTL interface, which indicates more efficient hole transport and suppressed interfacial recombination. Since recombination losses at interfaces often limit the performance of perovskite solar cells, the improved Nyquist response strongly validates the effectiveness of our optimization strategy. This observation is consistent with earlier reports,[72] reinforcing that electrical impedance spectroscopy provides crucial insight into charge dynamics and interfacial quality in PSCs.

4. Conclusion

The structural, mechanical, optoelectronic, and thermoelectrical characteristics of the lead-free halide perovskite A_3GaI_6 (A = Cs, K, Rb) are comprehensively investigated in this work using sophisticated computational tools like WIEN2k with the GGA-PBE, TB-mBJ, and TB-mBJ+SOC functionals. The resilience of A_3GaI_6 for real-world applications was demonstrated by the confirmation of its structural, thermodynamic, and mechanical stabilities through calculations of the Goldschmidt factor, formation energy (E_f), the convex-hull analysis (E_{hull}), and elastic constants (A = Cs, K, Rb). The calculated direct band gaps of 2.06/1.88 eV for Cs_3GaI_6, 1.83/1.65 eV for K_3GaI_6, and 1.94/1.76 eV for Rb_3GaI_6 (TB-mBJ/TB-mBJ+SOC) indicate favorable optical transitions within the visible to near-infrared region, which is consistent with the carrier-density and Bader-charge analyses showing that the Ga–I framework governs the electronic transport while the A-site cations modulate the charge distribution; consequently, the stronger charge transfer and higher carrier density in K_3GaI_6 and Rb_3GaI_6 support their more efficient carrier generation and transport compared with Cs_3GaI_6. K_3GaI_6 possesses the most appropriate bandgap (≈1.65 eV with TB-mBJ+SOC) among these compounds, characterized by lower carrier effective masses and enhanced electron and hole mobilities, which indicate more efficient charge transport. Additionally, its elevated static dielectric constant implies stronger dielectric screening and improved separation of photogenerated carriers. K_3GaI_6 is particularly promising for effective solar energy harvesting in comparison to its Cs-and Rb-based competitors. Exploiting DFT-derived inputs, SCAPS-1D simulations of a sixteen n-i-p K_3GaI_6-based perovskite solar cell yield efficiencies ranging from 19.48% to 22.48%, with the AZO/STO/K_3GaI_6/Zn_2P_2 configuration attaining the highest PCE, due the good alignment between PVK and transport layers in addition the physical proprieties of STO (ETL) and Zn_2P_2 (HTL). After optimization the selected configuration achieves a remarkable efficiency of 27.19%, underscoring its potential as a high-performance photovoltaic absorber. Collectively, these results not only establish a solid theoretical foundation for the experimental synthesis and exploration of K_3GaI_6, but also pave the way for its integration into next-generation optoelectronic and energy-harvesting devices. Moving forward, experimental realization and further optimization of K_3GaI_6-based materials will be critical to unlocking their full potential in renewable energy and advanced electronic technologies.

Conflicts of interest

The authors have no conflicts of interest to declare.

Data availability

All data supporting the findings of this study are included in the manuscript. Additional data, if required, can be provided upon reasonable request.

Supplementary information (SI) is available. See DOI: https://doi.org/10.1039/d5ra09544a.

Acknowledgements

Deanship of Scientific Research, Vice Presidency for Graduate Studies and Scientific Research, King Faisal University, Saudi Arabia [Grant No.: KFU261138].

References

1 M. W. Alam, *Breaking Boundaries: Pioneering Sustainable Solutions through Materials and Technology*, Springer Nature Singapore, Singapore, 2025.
2 M. Y. Khan, M. A. Jehangir, N. Israr, A. Hassan, U. Younis, J. Khan, M. Khan, A. Khan and A. Al Souwaileh, *Phys. B Condens. Matter*, 2025, **707**, 417150.
3 A. I. Shimul, B. Chandra Biswas, A. Ghosh, H. A. Alrafai and A. A. Hassan, *Sol. Energy Mater. Sol. Cells*, 2025, **293**, 113838.
4 A. I. Shimul, A. T. M. S. Islam, A. Ghosh, M. M. Hossain, S. A. Dipa and R. J. Ramalingam, *Comput. Mater. Sci.*, 2025, **250**, 113701.
5 NREL, Best Research-Cell Efficiencies, 2024, https://www.nrel.gov/pv/cell-efficiency.html.
6 A. N. Khan, N. U. Khan, M. Kaleem, M. Tanzeel, A. Nasir, A. Hosen, A. Akremi and I. Boukhris, *Solid State Sci.*, 2025, **168**, 108049.

7 A. I. Shimul, A. Ghosh, S. R. Sarker and H. A. Alturaifi, *RSC Adv.*, 2025, **15**, 7663–7681.
8 A. I. Shimul, A. Ghosh, M. F. Ahmed, A. S. Mugdho, Z. Hasan, N. S. Awwad and H. A. Ibrahium, *Langmuir*, 2025, **41**, 13655–13674.
9 A. I. Shimul, M. M. Haque, A. Ghosh, M. A. U. Sunny, S. O. Aljazzar, J. Y. Al-Humaidi and Y. E. Mukhrish, *J. Inorg. Organomet. Polym. Mater.*, 2025, **3**, DOI: 10.1007/s10904-025-03629-3.
10 S. Al-Qaisi, N. Iram, N. Sfina, A. Boutramine, H. R. Jappor, A. H. Alfaifi, H. S. Alzahrani, H. Rached, M. A. Ali and G. Murtaza, *Phys. B Condens. Matter*, 2025, **710**, 417239.
11 A. N. Khan, M. Kaleem, N. U. Khan, A. Nasir, A. Khan and M. Z. Abbasi, *Sol. Energy Mater. Sol. Cells*, 2026, **294**, 113922.
12 A. Boutramine, S. Al-Qaisi, S. Samah, A. K. Alqorashi, T. A. Alrebdi, M. Ezzeldien and M. F. Rahman, *J. Inorg. Organomet. Polym. Mater.*, 2024, **34**, 4133–4145.
13 Z. Xiao, W. Meng, J. Wang and Y. Yan, *ChemSusChem*, 2016, **9**, 2628–2633.
14 C. Wu, B. Du, W. Luo, Y. Liu, T. Li, D. Wang, X. Guo, H. Ting, Z. Fang, S. Wang, Z. Chen, Y. Chen and L. Xiao, *Adv. Opt. Mater.*, 2018, **6**(22), DOI: 10.1002/adom.201800811.
15 H. Murtaza, Q. Ain, J. Munir, H. M. Ghaithan, M. Ali, A. A. Ali Ahmed and S. M. Saif, *J. Phys. Chem. Solids*, 2024, **190**, 111934.
16 W. Zheng, X. Gan, D. Du, Y. Wang, S. Dai, L. Guo and H. Liu, *J. Wuhan Univ. Technol. Mater. Sci. Ed.*, 2023, **38**, 520–529.
17 A. Rakhmatullin, M. S. Molokeev, G. King, I. B. Polovov, K. V. Maksimtsev, E. Chesneau, E. Suard, R. Bakirov, F. Šimko, C. Bessada and M. Allix, *Inorg. Chem.*, 2021, **60**, 6016–6026.
18 G. Morrison, L. W. Masachchi, H. B. Tisdale, T. Chang, V. G. Jones, K. P. Zamorano, L. S. Breton, M. D. Smith, Y.-S. Chen and H.-C. zur Loye, *Dalt. Trans.*, 2023, **52**, 8425–8433.
19 A. Crovetto, A. Hajijafarassar, O. Hansen, B. Seger, I. Chorkendorff and P. C. K. Vesborg, *Chem. Mater.*, 2020, **32**, 3385–3395.
20 A. K. Baranwal, H. Masutani, H. Sugita, H. Kanda, S. Kanaya, N. Shibayama, Y. Sanehira, M. Ikegami, Y. Numata, K. Yamada, T. Miyasaka, T. Umeyama, H. Imahori and S. Ito, *Nano Converg*, 2017, **4**(1), DOI: 10.1186/s40580-017-0120-3.
21 V. G. Tyuterev and N. Vast, *Comput. Mater. Sci.*, 2006, **38**, 350–353.
22 C. L. Fu and K. M. Ho, *Phys. Rev. B*, 1983, **28**, 5480–5486.
23 F. Elfatouaki, O. Farkad, R. Takassa, S. Hassine, O. Choukri, A. Ouahdani, E. A. Ibnouelghazi, D. Abouelaoualim and A. Outzourhit, *Sol. Energy*, 2023, **260**, 1–10.
24 M. Y. Khan, M. A. Jehangir, I. E. Lee, Q. Wali, T. Usman, L. Xiaojie and A. Al Souwaileh, *Chem. Phys. Impact*, 2025, **11**, 0–10.
25 M. Jamal, M. Bilal, I. Ahmad and S. Jalali-Asadabadi, *J. Alloys Compd.*, 2018, **735**, 569–579.
26 M. Burgelman, P. Nollet and S. Degrave, *Thin Solid Films*, 2000, **361**, 527–532.
27 E. Dunlop, F. Fabero, G. Friesen, W. Herrmann, J. Hohl-Ebinger, H.-D. Mohring, H. Mullejans, A. Virtuani, W. Warta, W. Zaaiman, S. Zamini and N. Taylor, *Guidelines for PV power measurement in industry*, 2010.
28 V. M. Goldschmitdt, *Naturwissenschaften*, 1926, **14**, 477–485.
29 C. J. Bartel, C. Sutton, B. R. Goldsmith, R. Ouyang, C. B. Musgrave, L. M. Ghiringhelli and M. Scheffler, *Sci. Adv.*, 2019, **5**, 1–9.
30 K. Momma and F. Izumi, *J. Appl. Crystallogr.*, 2011, **44**, 1272–1276.
31 S. Al-Qaisi, N. Iram, S. Samah, A. K. Alqorashi, A. I. Aljameel, T. A. Alrebdi, Z. Abbas, S. Bouzgarrou, M. F. Rahman and A. S. Verma, *J. Comput. Chem.*, 2024, **45**, 1576–1586.
32 A. Boutramine, S. Al-Qaisi, N. Algethami, S. Tastift, A. H. Alfaifi, H. S. Alzahrani, H. Chaib, H. R. Jappor and H. Rached, *Phys. B Condens. Matter*, 2025, **711**, 417280.
33 H. Ahmed, S. Mukhtar, S. Agathopoulos and S. Z. Ilyas, *Phys. B Condens. Matter*, 2022, **640**, 414085.
34 S. Ghosh, M. Akhtaruzzaman and M. M. Uddin, *Mater. Today Commun.*, 2025, **48**, 113524.
35 R. Ali, Z. G. Zhu, Q. B. Yan, Q. R. Zheng, G. Su, A. Laref, C. S. Saraj and C. Guo, *ACS Appl. Mater. Interfaces*, 2020, **12**, 49636–49647.
36 M. Born, *J. Chem. Phys.*, 1939, **7**, 591–603.
37 W. Voigt, *Taubner*, 1928, 962.
38 A. Reuss and Z. A. M. M., *J. Appl. Math. Mech. / Zeitschrift für Angew. Math. und Mech.*, 1929, **9**, 49–58.
39 S. F. Pugh, *Dublin Philos. Mag. J. Sci.*, 1954, **45**, 823–843.
40 Y. Nassah, A. Benmakhlouf, L. Hadjeris, T. Helaimia, R. Khenata, A. Bouhemadou, S. Bin Omran, R. Sharma, S. Goumri Said and V. Srivastava, *Bull. Mater. Sci.*, 2023, **46**, 55.
41 A. I. Shimul, S. R. Sarker, A. Ghosh, M. T. uz Zaman, H. A. Alrafai and A. A. Hassan, *Inorg. Chem. Commun.*, 2025, **179**, 114737.
42 C. Gao, J. Zhu, S. Ye, M. Li, H. Wang and J. He, *J. Eur. Ceram. Soc.*, 2025, **45**, 116878.
43 X. Q. Chen, H. Niu, D. Li and Y. Li, *Intermetallics*, 2011, **19**, 1275–1281.
44 M. K. Masood, K. Chaoui, W. Khan, A. A. Awadh Bahajjaj, S. Bibi, A. Kanwal, C. Rania, Y. Bilal and J. Rehman, *Mater. Sci. Semicond. Process.*, 2025, **188**, 109214.
45 C. Zener, *Phys. Rev.*, 1936, **49**, 122–127.
46 F. D. Murnaghan, *Proc. Natl. Acad. Sci. U. S. A.*, 1944, **30**, 244–247.
47 M. E. Fine, L. D. Brown and H. L. Marcus, *Scr. Metall.*, 1984, **18**, 951–956.
48 A. Boutramine, S. Al-Qaisi, N. Sfina, L. A. Lamine, H. Chaib, M. Archi, O. Alsalmi and S. Rabhi, *Surfaces and Interfaces*, 2025, **72**, 107269.
49 S. Iqbal, G. M. Mustafa, M. Asghar, N. A. Noor, M. W. Iqbal, A. Mahmood and Y. H. Shin, *Mater. Sci. Semicond. Process.*, 2022, **143**, 106551.
50 R. Charif, R. Makhloufi, S. C. Mouna, A. Chadli, A. Barkat and M. Nouiri, *Phys. Scr.*, 2024, **99**, 1–24.
51 Y. Naik, D. Mehta, P. R. Parmar and P. B. Thakor, *Phys. B Condens. Matter*, 2024, **673**, 415499.
52 W. Tang, E. Sanville and G. Henkelman, *J. Phys. Condens. Matter*, 2009, **21**(8), DOI: 10.1088/0953-8984/21/8/084204.

53 L. Benahmedi, A. Besbes, R. Djelti, S. Moulebhar, A. Aissani and S. Bendehiba, *Sol. Energy*, 2025, **300**, 113860.
54 R. L. Milot, R. J. Sutton, G. E. Eperon, A. A. Haghighirad, J. Martinez Hardigree, L. Miranda, H. J. Snaith, M. B. Johnston and L. M. Herz, *Nano Lett.*, 2016, **16**, 7001–7007.
55 G. Folpini, L. Gatto, D. Cortecchia, M. Devetta, G. Crippa, C. Vozzi, S. Stagira, A. Petrozza and E. Cinquanta, *J. Chem. Phys.*, 2020, **152**(21), DOI: 10.1063/5.0008608.
56 O. R. Selmi, R. Makhloufi and R. Charif, *Phys. B Condens. Matter*, 2025, **716**, 417691.
57 A. I. Shimul, A. Ghosh, M. F. Ahmed, A. S. Mugdho, Z. Hasan, N. S. Awwad, H. A. Ibrahium, A. Islam, M. Hossain, S. Aktar, A. I. Shimul, B. C. Biswas, A. Ghosh, N. S. Awwad and H. A. Ibrahium, *Langmuir*, 2025, **41**, 13655–13674.
58 A. Islam, M. Hossain and S. Aktar, *Opt. Commun.*, 2025, **586**, 131916.
59 A. I. Shimul, B. C. Biswas, A. Ghosh, N. S. Awwad and H. A. Ibrahium, *Energy Technol.*, 2025, **202501240**, 1–20.
60 L. Yang, T. Xu, Z. Bai and S. Qin, *J. Phys. Chem. C*, 2023, **127**, 7492–7500.
61 S. Karthick, J. Bouclé and S. Velumani, *Sol. Energy*, 2021, **218**, 157–168.
62 N. K. Singh and A. Agarwal, *Energy Sources, Part A Recover. Util. Environ. Eff.*, 2023, **45**, 3087–3106.
63 E. N. Vincent Mercy, D. Srinivasan and L. Marasamy, *ACS Omega*, 2024, **4**, 4359–4376.
64 N. Rono, A. E. Merad, J. K. Kibet, B. S. Martincigh and V. O. Nyamori, *Energy Technol.*, 2021, **9**, 2100859.
65 P. Saha, S. Singh and S. Bhattacharya, *IEEE Trans. Electron Devices*, 2023, **70**, 1095–1101.
66 N. K. Singh, A. Agarwal and T. Kanumuri, *Energy Technol.*, 2022, **10**, 1–13.
67 K. Deepthi Jayan and V. Sebastian, *Sol. Energy*, 2021, **217**, 40–48.
68 F. Kherrat, L. Dehimi, H. Bencherif, M. M. A. Moon, M. K. Hossain, N. A. Sonmez, T. Ataser, Z. Messai and S. Özçelik, *Micro and Nanostructures*, 2023, **183**, DOI: 10.1016/j.micrna.2023.207676.
69 S. Rabhi, T. A. Hameed, S. Mayarambakam, M. K. Hossain and K. Sekar, *Heliyon*, 2024, **10**, e31138.
70 A. I. Shimul, S. R. Sarker, A. Ghosh, M. Moumita, N. L. Dey, K. U. Apu and N. S. Awwad, *New J. Chem.*, 2025, **49**, 14300–14321.
71 S. Rühle, *Sol. Energy*, 2016, **130**, 139–147.
72 N. Bouri, T. A. Geleta, K. W. Guji, A. Hammad, S. Rabhi and K. Nouneh, *J. Phys. Chem. Solids*, 2025, **207**, 112972.